Elsevier Editorial System(tm) for Lithos
Manuscript Draft

Manuscript Number: LITHOS4718R1

Title: Time-space focused intrusion of genetically unrelated arc magmas in the early Paleozoic Ross-Delamerian Orogen (Morozumi Range, Antarctica)

Article Type: Regular Article

Keywords: accretionary orogen; magmatic arc; intrusive complex; magma source; subduction erosion

Corresponding Author: Prof. Sergio Rocchi,

Corresponding Author's Institution: Università di Pisa

First Author: Sergio Rocchi, Prof.

Order of Authors: Sergio Rocchi, Prof.; Gianfranco Di Vincenzo, Dr.; Andrea Dini, Dr.; Maurizio Petrelli, Dr.; Simone Vezzoni, Dr.

Abstract: Growth of continental crust in accretionary orogenic belts takes place through repeated cycles of subduction-accretion of rock units from continental and oceanic magmatic arcs, supra-subduction zone backarcs and forearcs loaded with continent-derived materials. An ancient example relevant to magmatic arc accretion models is represented by the remnants of the Cambrian-Ordovician Ross Orogen in the Morozumi Range, Victoria Land (Antarctica). There, late Neoproterozoic phyllites host an intrusive complex which preserves a remarkably uncommon record of genetically unrelated magma pulses emplaced under a variable stress regime in a short time span: (1) a dominant K-feldspar-phyric granite, (2) fine-grained dioritic stocks and dykes, (3) a peraluminous granite; (4) a tonalitic-granodioritic dyke swarm. Laserprobe U-Pb zircon dates cluster at late Cambrian times for all these units, yet they carry differential cargoes of relict cores. Unique geochemical-isotopic signatures for both the less evolved magmas (diorite and dyke tonalite) and the most acidic ones (granite and peraluminous granite) indicate that each one of them originated from distinct sources at depth. Additionally, field relationships and chemical evolutionary trends testify for a variety of shallow level open-system processes, such as magma mingling/mixing between diorite and main granite magmas, as well as progressive incorporation of the host schists by the dyke tonalite magma. In summary, crustal growth in the Morozumi intrusive complex was contributed by fresh mantle magma issuing from the metasomatized mantle wedge, while the production of other melts did recycle different crustal portions/layers: the main granite derived from Grenville-age granulitic lower crust; the peraluminous granite from late Proterozoic upper crust; the tonalite magmas derived from subduction erosion-enriched subarc mantle and evolved by ingestion of local metasedimentary rocks. Overall, the Morozumi intrusive complex yields evidence for emplacement in the same site at the same time of magmas issuing from different sources that are usually found at different depth in the arc lithospheric section. A likely scenario to activate this specific mechanism of melt production is a subduction zone affected by subduction erosion.

Time-space focused intrusion of genetically unrelated arc magmas in the early Paleozoic Ross-Delamerian Orogen (Morozumi Range, Antarctica)

S. Rocchi[1], G. Di Vincenzo[2], A. Dini[2], M. Petrelli[3], S. Vezzoni[1]

1. Dipartimento di Scienze della Terra , Università di Pisa, Italy - tel: +390502215710, fax: +390502215800, email: sergio.rocchi@unipi.it

2. Istituto di Geoscienze e Georisorse, CNR, Pisa, Italy

3. Dipartimento di Fisica e Geologia, Università di Perugia, Italy

ABSTRACT

Growth of continental crust in accretionary orogenic belts takes place through repeated cycles of subduction–accretion of rock units from continental and oceanic magmatic arcs, supra-subduction zone backarcs and forearcs loaded with continent-derived materials. An ancient example relevant to magmatic arc accretion models is represented by the remnants of the Cambrian-Ordovician Ross Orogen in the Morozumi Range, Victoria Land (Antarctica). There, late Neoproterozoic phyllites host an intrusive complex which preserves a remarkably uncommon record of genetically unrelated magma pulses emplaced under a variable stress regime in a short time span: (1) a dominant K-feldspar-phyric granite, (2) fine-grained dioritic stocks and dykes, (3) a peraluminous granite; (4) a tonalitic-granodioritic dyke swarm. Laserprobe U-Pb zircon dates cluster at late Cambrian times for all these units, yet they carry differential cargoes of relict cores. Unique geochemical-isotopic signatures for both the less evolved magmas (diorite and dyke tonalite) and the most acidic ones (granite and peraluminous granite) indicate that each one of them originated from distinct sources at depth. Additionally, field relationships and chemical evolutionary trends testify for a variety of shallow level open-system processes, such as magma mingling/mixing between diorite and main granite magmas, as well as progressive incorporation of the host schists by the dyke tonalite magma. In summary, crustal growth in the Morozumi intrusive complex was contributed by fresh mantle magma issuing from the metasomatized mantle wedge, while the production of other melts did recycle different crustal portions/layers: the main granite derived from Grenville-age granulitic lower crust; the peraluminous granite from late Proterozoic upper crust; the tonalite magmas derived from subduction erosion-enriched subarc mantle and evolved by ingestion of local metasedimentary rocks. Overall, the Morozumi intrusive complex yields evidence for emplacement in the same site at the same time of magmas issuing from different sources that are usually found at different depth in the arc lithospheric section. A likely scenario to activate this specific mechanism of melt production is a subduction zone affected by subduction erosion.

Keywords: accretionary orogen; magmatic arc; intrusive complex; magma source; subduction erosion

1. Introduction

Magma generation in convergent settings is usually from multiple sources, including the mantle wedge, the overriding plate, and the subducting slab as well. The overriding plate can contribute as either a contaminant of uprising magmas (Davidson et al., 2005) or a direct source of melts from the upper/lower crust (Brown, 2013), and the juvenile underplates as well (Rocchi et al., 2009). The subducting lithosphere can contribute by direct partial melting (Defant and Drummond, 1990), addition to the mantle wedge of a subduction component via aqueous fluids/hydrous melts (Pearce and Peate, 1995), as well as via more massive, bulky processes such as subduction erosion (von Huene et al., 2004) and subduction of continental crust (Hacker et al., 2011). Actual arc magmas are thus the outcome of a bouquet of processes (Davidson et al., 2005), including source melting degree and regime (equilibrium/ disequilibrium), fractional crystallization, (possibly accompanied by assimilation), and hybridization between different magmas, from deep crustal to emplacement levels (Brown, 2013). In accretionary orogens, processes of mantle modifications can occcur every time subduction takes over slab rollback and backarc opening. This variety of materials and processes makes orogenic igneous complexes a rich source of information, yet difficult to disentangle.

A magmatic arc that underwent most of these petrogenetic processes in a convergent accretionary setting was active during the early Paleozoic at the paleo-Pacific margin of Gondwana in Antarctica. The Cenozoic uplift linked to the West Antarctic rift system led to prominent exposures of arc deep-seated terrains in clean outcrops. Among these, the Morozumi Range igneous complex in northern Victoria Land is made of a variety of intrusive rocks with well exposed mutual chronological, petrological and structural relationships. Field observations, coupled with chemical data, isotopic geochemistry and geochronology, led to the reconstruction of a scenario that shed light on potential modalities of magma formation and evolution in magmatic arcs. Additionally, new implications on the evolution of the Antarctic margin of Gondwana in Cambrian-Ordovician time are proposed to update current models.

2. Geological setting

Today's Transantarctic Mountains represent the roots of an orogen exposed on the shoulder of the Cretaceous–Cenozoic West Antarctic rift system (Rossetti et al., 2006a). The orogen dates back to Neoproterozoic-late Paleozoic times, when the large-scale subduction-related crustal accretion known as the Ross-Delamerian(-Tyennan) Orogeny occurred in the frame of the convergence between Paleo-Pacific oceanic lithosphere and the Gondwana continental margin. Remnants of this orogen are now exposed along 3500 km of the Transantarctic Mountains, as well as in southeastern Australia, Tasmania and the South Island of New Zealand (Boger and Miller, 2004; Flöttmann et al., 1993; Foden et al., 2006; Gibson and Ireland, 1996; Glen, 2013; Stump, 1995).

The begininning of the Ross-Delamerian orogenic cycle, as recorded by the age of the oldest magmatism, has long been debated. A possible diachronous inception of magmatism has been postulated based on the ages of oldes igneous rocks of 514 Ma in Australia (Foden et al., 2006), of 540-520 Ma in Victoria Land (Allibone and Wysoczanski, 2002; Giacomini et al., 2007; Rocchi et al., 2004), and of around 550 Ma in central Transantarctic Mountains (Encarnación and Grunow, 1996), with detrital zircon ages and glacial clasts reaching 580-590 Ma (Goodge et al., 2012; Goodge et al., 2004). However, there is no robust evidence that the Ross Orogeny and subduction-related arc magmatism started before c. 540-530 Ma, and the diachronous starting of the orogenic cycle in Antarctica and Australia has recently been questioned (Gibson et al., 2011; Turner et al., 2009). Nevertheless, the age and geochemical patterns of intrusive rocks suggest oblique convergence along a tectonically segmented margin (Encarnación and Grunow, 1996; Goodge, 2002; Goodge et al., 2012; Goodge et al., 2004; Rocchi et al., 1998; Stump et al., 2006). The latest magmas emplaced in the Ross Orogen are about 480 Ma, and evidence for younger (460-440 Ma) amagmatic contractional tectonic activity in Victoria Land is likely related to the early stages of the formation of the Lachlan Fold Belt (Di Vincenzo et al., 2007), which is best developed in southeastern Australia (Glen et al., 2007).

A key segment of the Transantarctic Mountains is their Pacific Ocean-Ross Sea termination in northern Victoria Land (Fig. 1), commonly considered the along-strike continuation of Australia in Antarctica (Finn et al., 1999; Flöttmann et al., 1993; Stump et al., 1986) and described as an assembly of three fault-bounded terranes (Bradshaw et al., 1985; Gibson and Wright, 1985; Kleinschmidt and Tessensohn, 1987; Stump et al., 1983; Weaver et al., 1984), namely, from the continent toward the ocean: (i) the metamorphic Wilson terrane intruded by

Cambrian-early Ordovician plutonic rocks (Bomparola et al., 2007; Rocchi et al., 1998; Stump, 1995), (ii) the volcanic-sedimentary Bowers terrane (Crispini et al., 2007; Weaver et al., 1984) and (iii) the Robertson Bay terrane, with thick, weakly metamorphosed turbiditic sequences intruded by Devonian granites (Di Vincenzo et al., 2014; GANOVEX TEAM, 1987; Rossetti et al., 2006b).

Recent works (Bracciali et al., 2009; Federico et al., 2006; Ferraccioli et al., 2009; Ferraccioli et al., 2002; Gemelli et al., 2009; Rocchi et al., 2003; Roland et al., 2004; Tessensohn and Henjes-Kunst, 2005) led to an updated model of the Ross Orogeny in Victoria Land (Rocchi et al., 2011). In this new Cambrian scenario, the convergent Paleo-Pacific margin of Gondwana consisted of a main continuous subduction zone coupled with local, transient subduction zones related to a more or less continuous ribbon of outboard pieces of stretched forearc regions. Thus, the Victoria Land portion of the Ross orogenic belt is inferred to derive neither by collision against the margin of large continents/exotic continental blocks, nor by the unique accretion of forearc oceanic lithosphere. Rather, the transient coupling between the lower and upper plates generated multiple docking of small-sized continental fragments with restricted periods of co-existence of double subduction zones. The Ross Orogen in Victoria Land was thus the result of alternate episodes of advancing and retreating subduction zone(s). Within the key segment of Victoria Land, a critical area is thus represented by the boundary zone between the Wilson arc and the forearc ribbon which underwent detachment and re-accretion to the arc (Rocchi et al., 2011). Here, the intrusive complex of the Morozumi Range (Fig. 1) recorded multiple episodes of magma emplacement in the same site, in a short time, under a variable stress regime.

3. The Morozumi Range intrusive complex - field and petrographic features

The Morozumi Range intrusive complex is hosted by the Morozumi phyllites (Fig. 2a), a metasedimentary unit with a late Neoproterozoic maximum deposition age, and characterised by a regionally extensive subvertical foliation, locally overprinted by contact metamorphic effects up to 600°C at 0.2 GPa [Engel, 1984 #2916]. The Morozumi phyllites are unconformably overlain by the Permian continental-fluvial sandstones of the Beacon Supergroup, which are in turn conformably overlain by the lava flows and intruded by the columnarly jointed sills of the early Jurassic Ferrar large igneous province. The intrusive complex consists of a set of magmatic bodies with variable composition and well exposed intrusive relationships (Fig. 2). Seven different intrusive units are defined in the field based on their petrographic features (see summary in Table 1).

Morozumi granite. The Morozumi granite is by far the largest intrusive unit of the complex, extending north-south for ca. 16 km, with an east-west width of 1 km to 6 km (Fig. 1). The contacts against the country rock are subvertical, so that the intrusion has the overall aspect of a subvertical large tabular body (Fig. 2a). It mostly consists of a porphyritic monzogranite with white to pink K-feldspar megacrysts (up to 5 cm, Fig. 2b) set in a medium-grained groundmass with 10-15 vol% red-brown biotite, and allanite as a common accessory phase. K-feldspar megacrysts locally define a subvertical igneous foliation and lineation, parallel to the host schist foliation.

Morozumi diorite. The southwesternmost part of the intrusive complex include mafic stocks and dykes intruding the Morozumi granite (Fig. 2m). The contact between the mafic and felsic units is either pillowing-sharp (Fig. 2n) or diffuse (Fig. 2h), suggesting coeval emplacement relationships. The Morozumi diorite is an equigranular, fine- to medium-grained quartz-diorite characterized by the occurrence of both biotite and green amphibole totalling up to 50 vol%.

Morozumi granodiorite. This unit is a minor network of irregular bodies with fine-grained texture and high biotite content (about 20 vol%). Contacts against the Morozumi Granite are either sharp or diffuse, with evidence of progressive passage to the Morozumi granite on one side and to the Morozumi diorite on the other side (Fig. 2h).

Morozumi dykes. The intrusive complex includes several tonalitic/granodioritic dykes which, on the basis of field occurrence, have been grouped into: (i) *eastern dykes,* (ii) *western dykes* and (iii) *crestal dykes.* The *eastern dykes* are subvertical tabular bodies conformably intruding and interlayered with the foliation of the host Morozumi phyllites (Fig. 2a, d). Dykes are medium-grained foliated tonalites and granodiorites with 5 to 10 vol% biotite ± muscovite. At the northernmost tip of the range, the fine- to medium-grained thin peraluminous leucosyenogranite dykes with muscovite ± garnet or tourmaline intruded into the metasedimentary host are strongly foliated and boudinaged (Fig. 2d, g). Deformation style sometimes grades to mylonitic, with asymmetric boudins indicating a west-side-up movement (Fig. 2g). In other instances, fragments or streaks of Morozumi phyllites are stretched, dismembered and dispersed in the host dyke (Fig. 2f). These relationships and the parallel emplacement of eastern dykes and the main Morozumi granite body suggest the latter intruded soon after the intrusion of the dykes that were still amid the solidification process. The *western dykes* are west-dipping tabular bodies intruding the Morozumi granite at high angle with the igneous foliation, and the Jupiter granite as well. When intruding the Morozumi granite, dykes are fine-grained foliated tonalites with about 15 vol% biotite. Dykes intruding into the Jupiter granite are medium-grained granodiorites with about 20 vol% biotite and up to 5 vol% muscovite. Western dikes intrude on ramps that crosscut the vertical foliation of the granite host, with some ductile deformation of the granite foliation that should thus have been not completely cooled down at the time of dyke emplacement. Kinematic indicators for this ductile deformation indicate a top-the-east relative movement. The *crestal dykes* are tabular intrusions cropping out in the summit part of the ridge: gently west-dipping tabular bodies, locally cutting the intrusive foliation of the the Morozumi granite; they are fine-to medium-grained leucomonzogranites to leucogranodiorites with less than 5 vol% biotite along with minor muscovite. In the crestal zone of the range, the dykes crosscut the subvertical igneous foliation with knife-sharp contacts (Fig. 2c) and top-to-the-east relative movement, as testified by mylonitic shear at the contact (Fig. 2e), the same relative movement observed for the western dykes. In summary, in the eastern side of the complex the emplacement of the granite appears contemporaneous to slightly later than the dyke emplacement, while in the western side and the topmost outcrops the granite foliation is crosscut by the dykes that thus were emplaced when the granite was solidifying (west) or solid (crest).

Jupiter granite. This intrusive unit is named after the main spectacular outcrop in the southern part of the Jupiter Amphitheatre, where a medium- to coarse-grained massive body of peraluminous biotite+muscovite-monzogranite neatly crosscut the country rock (Fig. 2i). Field relationships with the Morozumi granite have not been observed, while peraluminous syenogranitic massive bodies of the Jupiter granite unit are intruded by tabular bodies along the western flank of the intrusive complex (western tabular intrusions). Here the Jupiter medium to coarse-grained granite contains igneous muscovite up to 5-10 vol%.

Morozumi leucogranites/aplites. Scattered minor bodies of fine- to medium-grained, equigranular peraluminous, muscovite ± garnet or tourmaline-bearing leucosyenogranites are found both within the Morozumi granite and at the contact between the granite and the host schists.

4. Analytical methodologies

Major elements (Table 2) were determined by X-ray fluorescence (XRF-ARL 9400XP) on glass beads, at Dipartimento di Scienze della Terra, Università di Pisa, with precision between 1% and 4% RSD for most elements, except TiO_2, MnO, CaO, Na_2O, (5–8% RSD) (Tamponi et al., 2003). Trace elements (Table 2) were determined by inductively coupled plasma-mass spectrometry (ICP-MS, VG PQII Plus) (Rocchi et al., 2002) at Dipartimento di Scienze della Terra, Università di Pisa, after dissolution with HF-HNO_3 mixture in screw-top PFA vessels on a hotplate at 120 °C. Analyses were performed by external calibration using the matrix-matching geochemical reference sample BE-N. The correction procedure includes blank subtraction, instrumental drift correction (Rh-Re-Bi internal standardization and repeated analysis of a drift monitor), and oxide-hydroxide interference correction. Precision, evaluated by replicate dissolutions and analyses of in-house and international silicate rock reference samples, is generally between 2% and 5% RSD for most elements, except Cr, Ni, Pb (6–11% RSD). Zirconium was determined via XRF on pressed powder pellets.

Sr and Nd isotopic compositions were determined using a Finnigan MAT 262V multicollector mass spectrometer at Istituto di Geoscienze e Georisorse-CNR, Pisa, following separation of Sr and Nd using conventional ion exchange procedures. Measured $^{87}Sr/^{86}Sr$ ratios have been normalized to $^{86}Sr/^{88}Sr = 0.1194$; $^{143}Nd/^{144}Nd$ ratios to $^{146}Nd/^{144}Nd = 0.7219$. During the course of this study, the external reproducibility for NIST-SRM987 and La Jolla Nd standards were $^{87}Sr/^{86}Sr = 0.710250\pm24$ and $^{143}Nd/^{144}Nd = 0.511858\pm14$ (2 SD), respectively. The measured Nd isotopic ratios have been adjusted to a value for La Jolla standard of $^{143}Nd/^{144}Nd = 0.511850$.

Geochronological data were obtained by zircon U-Pb analyses. After crushing and sieving, zircons were concentrated from the 160-250 μm grain sizes using standard separation techniques. About 100 zircons for each sample were cast in epoxy resin and polished to a 0.3 μm alumina paste finish to expose mid-section of crystals. Crystal for geochronological analyses have been selected on the basis of textural observations related to inclusions, occurrence/type of core and/or rim, zoning, etc carried out by Scanning Electron Microscopy-Cathodoluminescence (SEM-CL) imaging by a Philips XL30 SEM at Dipartimento di Scienze della Terra, Università di Pisa. U-Pb analyses by Laser Ablation-Inductively Coupled Plasma-Mass Spectrometry (LA-ICP-MS) were performed at Dipartimento di Fisica e Geologia, Università di Perugia (Italy) (Alagna et al., 2008) using a Thermo Electron X7 ICP-MS coupled to a New Wave UP213 frequency quintupled Nd:YAG laser. U-Pb zircon analyses were calibrated with standard zircon 91500 using a spot size of 25 μm and zircon GJ1 has been used as quality control. The error associated with the standard reproducibility has been combined quadratically with the counting statistics of each analysis.

5. Geochronological data

In order to define the temporal evolution for the emplacement of the different intrusive units, as well as to investigate differential source inheritance in different magmas, seven samples of magmatic rocks along with one sample of the metamorphic host rock have been investigated for U-Pb zircon geochronology (Table SM1).

Morozumi granite. Data from zircons with a well-preserved oscillatory magmatic zoning give a concordia age of 493.7±8.7 Ma (with decay-constant errors ignored, probability of concordance = 0.995, Fig. 3a), interpreted as the emplacement age for Morozumi granite. Zircons with ghost zoning, i.e. areas where typical igneous zoning is lacking or poorly defined, yielded younger ages and are interpreted as related to post-igneous reworking. The oldest ages clustering around 1000 Ma (Grenville-like, Fig. 4) are from three zircon cores lighter than the rim, with truncated zoning, interpreted as relict cores.

Morozumi diorite. The zircon yield was poor, comprised of tiny, elongated crystals with no well-defined oscillatory zoning and the obtained data does not allow to constrain the time of emplacement. Nevertheless, the clear hot mingling relationships with Morozumi granite (Fig. 2n) led to infer a coeval emplacement timing.

Morozumi granodiorite. Zircons with well-defined zoning have a concordia age, obtained from 5 points analysis and excluding reworked zircon areas, of 485.3±5.4 Ma (probability of concordance = 0.88, Fig. 3b). Older age clusters between 520 Ma and 650 Ma are obtained from zircons with unzoned light cores, interpreted as reworked areas. Two data points on cores give Grenvillian ages, and a single analysis yielded a Proterozoic age (Fig. 4).

Morozumi dykes. Eastern dyke. Zircon crystals are characterized by a dark core and a light rim. A few crystals have an innermost light core, and some others show oscillatory or convoluted zoned cores. Five analyses of light rims provided a Concordia Age of 496.7±6.8 Ma (probability of concordance = 0.92, Fig. 3c), interpreted as the emplacement age. Three additional analyses of cores give ages between ca. 550 and 1900 Ma (Fig. 4). *Western dyke.* The zircon yield was modest and only 12 analyses were performed for a western dyke sample. These zircons are unzoned or show convolute/ghost zoning. Six analyses (from both cores and rims) range between 437±11 Ma and 573±14 Ma. The lack of any clear magmatic zoning suggests post-magmatic reworking for these zircon crystals. Five additional analyses from relict cores (973±23 to 1120±25 Ma) indicate the occurrence a Grenville-age component in the magma source (Fig. 4).

Jupiter granite. Once data from zircons with ghost zoning were discarded, five zircon crystals from sample JG1 with well-defined oscillatory zoning give a concordia age of 495.3±5.7 Ma (probability of concordance = 0.78, Fig. 3d), interpreted as the emplacement age. Sample JG2 did yield just a few crystals, with two cores giving Grenvillian ages (Fig. 4).

Morozumi phyllites. The studied sample has been collected in the southern part of the Morozumi Range, far from contacts against igneous rocks, to study a pristine sample not affected by thermal effects, that are indeed not been observed in both thin sections and SEM-CL zircon images. The only overgrowth observed has a $^{206}Pb/^{238}U$ age indistinguishable from that of the core, within the same crystal (2299±80 vs. 2293±81 Ma, respectively). The pristine characters of zircons allow to infer the youngest concordant zircon ages (571±22 and 601±22 Ma) as the oldest limit for the deposition of this unit, at the very end of the Neoproterozoic. Younger Cambrian deposition age for the Morozumi phyllites are inferred, based on unpublished dtrital zircon ages [Henjes-Kunst, 2003 #2569]. A deposition age at the boundary between latest Neoproterozoic and Cambrian (c. 545 Ma) is inferred based on detrital zircon ages for the Berg Group and the Priestley Formation of the Wilson terrane, as well as the Molar Formation of the Bowers terrane (Adams et al., 2013).. Our data, plotted in a cumulative probability plot (Fig. 4) shows a wide range of ages, with well-defined peaks slightly older than 600 Ma (< 20% of zircons) and around Grenville age (~ 40%); three minor peaks occur at Paleoproterozoic-Archean times (total of ~ 40%). The lack of thermal imprints or metamorphic overgrowths calls for a mechanism of cooling of the intruded magmas with no significant conductive heating of the country rock.

In summary, individual intrusive units provide indistinguishable emplacement ages for the main granite (493.7±8.7 Ma), the eastern dykes (496.7±6.8 Ma) and the peraluminous granite (495.3±5.7 Ma). Geochronological data for the Morozumi diorite does not define an emplacement age, yet field relations indicate contemporaneous emplacement with Morozumi main granite (Fig. 2n). The Morozumi granodiorite provides a slightly younger nominal age of 485.3±5.4 Ma, although still indistinguishable at 2σ level from those of the other units, in close agreement with field observations (Fig. 2h). For the Morozumi western dykes, the emplacement age could not be defined geochronologically, nevertheless field relations with the Morozumi granite (the dykes cut the granite igneous foliation at high angle with ductile deformation of the granite) suggest once again an emplacement age almost coeval with the Morozumi granite. In summary, a short time interval of no more than a few Ma around ca. 495 Ma is inferred for the emplacement of the whole Morozumi intrusive complex.

As for the relict zircon signatures, all the intrusive units (granite, granodiorite, dykes, peraluminous granite) contain relict cores with Neoproterozoic and Mesoproterozoic (Grenville) ages, along with rare Paleoproterozoic cores. A couple of Archean cores were found only in the peraluminous Jupiter granite.

6. Geochemical and isotopic data

The lithological diversity of the Morozumi intrusive complex is mirrored by large variabilities in the major element compositions. The Total Alkali-Silica (TAS) diagram readily shows that the whole data set splits into two main subalkaline trends with different levels of alkali enrichment (Fig. 5). The Morozumi diorite-granodiorite-granite samples define a roughly linear trend barely reaching the granite field. At lower alkali contents, the samples from

Morozumi dykes define a separate roughly linear trend from the granodiorite well into the granite field. Both trends have slopes that cut across the usual boundaries between magmatic associations, in contrast with the typical magmatic evolution in closed systems.

The trace element distributions of the most mafic rocks from the two trends share common features, such as a significant enrichment for the most incompatible elements, along with marked negative anomalies for Nb-Ta and minor for Ti (Fig. 6). Besides those similarities, the patterns also show some differences: the Morozumi diorites, despite having a silica content higher than that of the most mafic Morozumi tonalite dyke, feature a higher enrichment in rare earth elements (REE), most marked for heavy REE.

Among mafic igneous rocks from the early Paleozoic Ross Orogen of northern Victoria Land, the Morozumi diorite display strong affinity to potassic rocks such as the Abbott gabbro and the Vegetation lamprophyres, representing mantle-derived magmas emplaced in the late orogenic to postcollisional stage (Di Vincenzo and Rocchi, 1999; Rocchi et al., 2009). Among igneous rocks of comparable compositions, the Morozumi tonalite dyke has a trace element distribution quite similar to that of the Confusion tonalite, a calk-alkaline unit characterizing a tectonomagmatic stage earlier than the Abbott and Vegetation potassic events (Rocchi et al., 2004).

The Sr and Nd isotopic systematics help clarifying the petrologic affinities of the Morozumi igneous rocks (Fig. 7). The Morozumi diorite has Sr and Nd isotopic ratios higher and lower than those of the Abbott gabbro, respectively, and definitely similar to those of the Vegetation lamprophyres (Di Vincenzo and Rocchi, 1999): the Morozumi diorite has thus trace element and isotopic features typical of a potassic, post-collisional magma. The Morozumi tonalite dyke samples have scattered Sr isotopic compositions, making it difficult any direct comparison (see further on).

The most felsic rocks of the two trends plot separately: a gap of 5 wt% SiO_2 separates rocks with the same alkali (and K) contents. The Jupiter granite differs from all the other Morozumi felsic rocks owing to its peraluminousity (Alumina Saturation Index: 1.1-1.2), and low Nd isotopic ratios, coupled at odd with relatively low Sr isotopic ratios (< 0.711).

7. Discussion - Petrogenetic issues

The two roughly parallel compositional trends (Fig. 5) follow possible evolutionary paths starting from two different parental magmas. The slopes of these trends, cutting across the usual boundaries of magmatic associations (Fig. 5), coupled with Sr-Nd isotope data (Fig. 7), rule out closed-system compositional evolution for both trends. The 5 wt% SiO_2 gap separating felsic rocks with the same alkali (and K) contents, also lend support to the hypothesis of a separate origin for the compositional groups of felsic rocks. Therefore, simple petrogenetic evolutionary relationships among the various igneous units are precluded and a minimum number of different magmas had to be involved in the genesis of the Morozumi complex, namely: a mafic potassic dioritic melt (Morozumi diorite), a mafic tonalitic melt (Morozumi mafic dykes), a felsic metaluminous granitic melt (Morozumi granite), as well as a felsic peraluminous granitic melt (Jupiter granite). Additionally, a possible high-silica metaluminous melt could have existed (Morozumi felsic dykes), yet field relationships indicate that a mass contribution of the Morozumi phyllites to the compositional variability of the dykes has to be taken into account (Fig. 2f). In the following we are going to first discuss the origin of the different melts at source depth, then their interaction/evolution at shallower levels during ascent/emplacement.

7.1. What type of mantle? Origin of mafic "parental" melts:

Morozumi diorite. The reconstruction of the type of mantle source activated for the production of the most mafic Morozumi magmas is hampered by the absence of any rock which could be assumed as representative of a primary mantle melt. Even the least silicic Morozumi diorite samples are indeed quite evolved, having an overall andesitic composition. Nevertheless, an origin from remelting of basaltic rocks at depth in the crust is not supported, owing to the lack of any evidence for Ross basaltic magmatism in the area. The Morozumi diorites are therefore best considered as representative of mantle melts which underwent some differentiation, potentially including open-system processes. Indeed, simple fractional crystallization is not sufficient to explain the isotopic variability of the diorite samples. Also the overall compositional trend encompassing mingled rocks (the Morozumi granodiorite show evidence for mingling-mixing relationships between the Morozumi diorite and granite melts; Fig. 2h) lend neat support to the occurrence of open-system interaction processes. To back-reconstruct the possible chemical and isotopic composition of the parental basaltic melt, a modeling of assimilation and fractional crystallization (AFC) has been run out (DePaolo, 1981). In order to derive the parameters to be used for trace element and isotopic AFC modelling, preliminary mass balance calculations have been performed: the major element composition of the finest-grained and mafic Morozumi diorite (sample 23.12.05 DS7) has been obtained starting from a common high-Al Andean basalt (Wilson, 1989) via fractionation of 9 wt% orthopyroxene, 1 wt% clinopyroxene and 25 wt% plagioclase, plus the addition of about 23 wt% of a migmatitic leucosome, with mineral and migmatite compositions after similar gabbroic-dioritic rocks from the Wilson terrane (Di Vincenzo and Rocchi, 1999). The parameters thus obtained (mass fraction crystallised = M_{FC} = 0.35; ratio of the rate of assimilation to the rate of fractional crystallisation = a = 0.66) have been used to run AFC modelling for Sr-Nd systematics, obtaining values of $^{87}Sr/^{86}Sr_{(500\ Ma)}$ = 0.706 and $\varepsilon_{Nd(500\ Ma)}$ = -1 for a possible primitive Morozumi mafic melt. These values point out that the main Morozumi original mafic melt had to have geochemical and isotopic features which are enriched compared to common primitive arc basalts. These features could either derive from (i) metasomatic enrichment in the mantle wedge, or from (ii) refilling of a fractionating-assimilating magma pond at the mantle-crust interface (R-AFC) (O'Hara, 1977), which is likely to happen in a zone of underplating characterised by periodic or continuous input of fresh mantle magma; this process could potentially generate enriched compositions from non-enriched sub-arc mantle wedge. However, the Morozumi diorite has Sr and Nd contents that are above the threshold over which a metasomatically enriched source has necessarily to be invoked (Di Vincenzo and Rocchi, 1999). The zircon yield from the Morozumi diorite, although quite poor, allow to establish the absence of relict cores, further supporting the full-mantle origin of this magma. In conclusion, the original/parental Morozumi diorite melt had to derive from a metasomatized mantle wedge characterised by an $\varepsilon_{Nd(500\ Ma)}$ not higher than -1 and a $^{87}Sr/^{86}Sr_{(500\ Ma)}$ not lower than 0.706.

Morozumi tonalite. This unit does not include any rock which could be assumed as representative of a primary mantle melt. Even the least silicic rock samples are quite evolved, so their composition could in principle derive from several different processes. The composition of tonalite is not compatible with derivation from melting of metasedimentary material with protoliths such as pelites, greywackes or volcaniclastics (Fig. 8a). An alternative process is the chemical evolution of a mantle melt, which however should leave some traces of basic-intermediate products: the lack of products with SiO_2<65 wt% is in contrast with this hypothesis. Another alternative is the crustal contamination of the Morozumi diorite melt, which however conflicts with the observation that samples with the same $\varepsilon_{Nd(500\ Ma)}$ have a difference of 10 wt% in the SiO_2 content. On the other hand, the Morozumi tonalites are very similar to high-silica adakites for major elements composition as well as for their high La/Yb, low Yb, high Sr/Y and low Y (Fig. 8b). However, the adakites interpreted as products of young slab melting, as for their original definition (Defant and Drummond, 1990), usually have positive ε_{Nd} (Castillo, 2012), in opposition to the low ε_{Nd} of the Morozumi tonalite melt. Such a magma should therefore derive from melting of mafic material residing in the (lower?) crust. Remelting of an underplate made of Morozumi potassic diorite is not likely because the tonalite has much lower K content than the diorite; additionally, the observed ε_{Nd} values between -5 and -6 would require melting of evolved-hybrid diorite rather than diorite itself, but the observed hybridization process is limited, likely occurring en route to the emplacement level, and not at the underplate level. Another potential crustal basic source is represented by normal gabbros or basic amphibolites. Melting experiments (Sisson et al., 2005) indicate that the Na/K/Ca relationships of the Morozumi granodiorite/tonalite are matched by melting hornblende gabbro at high T (>925°C), yet these melts have SiO_2<60 wt%; using biotite- or quartz-bearing hornblende gabbro as a source and/or lowering the melting temperature yields products with higher SiO_2, comparable with Morozumi granodiorite/tonalite, but with somewhat higher K/Ca ratios (Fig. 8a). Melting experiments of amphibolites with alkali basaltic and island arc tholeiitic composition (Rushmer, 1991) yield melts with lower SiO_2 and higher Ca/Na ratios with respect to the Morozumi tonalite (Fig. 8a); on the other hand, "synthetic amphibolites" (a mix of hornblende, albite and quartz) at high T=975 °C give melts with a composition compatible with the Morozumi tonalite (Rushmer, 1991). Also the occurrence of even a few old zircons with variable Proterozoic ages helps ruling out simple young slab or underplate melting, rather supporting addition of some crustal material to the mantle wedge. The process responsible of such an addition could be ascribed to the category of subduction erosion that can also explain strong REE fractionation coupled with high Sr content without invoking subduction of young slab at garnet depth (Kay et al., 2005). Large-scale subduction erosion or even larger-scale subduction of small continental block(s) can bring into the mantle wedge crustal materials, which then exhumes due to slab roll-back, becomes incorporated into the overriding plate (Brun and Faccenna, 2008) and can contribute to melt generation.

7.2. What type of crust? Origin of felsic melts

The four types of felsic intrusive units of the Morozumi complex have very different sizes: the Morozumi granite is by far the most voluminous, constituting most of the mass of the intrusive complex; the Jupiter peraluminous granites are found in two main large outcrops; the Morozumi leucogranites represent very small, vein- or pod-like bodies; the Morozumi dykes with felsic composition are leucogranitic portions of tonalite-granodiorite dykes. The chemical and isotopic compositions of these four felsic rock types point out that they also have distinct origins.

The Jupiter granite and the vein-like Morozumi leucogranites have compositions typical of minimum melts from metasedimentary protoliths such as greywacke or pelite rocks (Fig. 8a). These minor units have Sr-Nd compositions displaced from the main trend towards lower Sr isotopic ratios (Fig. 7), as observed elsewhere for melting occurring in disequilibrium conditions (Farina et al., 2014; Farina and Stevens, 2011; Harris and Ayres, 1998). Relict zircons show an age spectrum including scattered evidence for recycling of early Proterozoic and Archean material. In synthesis, the source that can be inferred for the Jupiter granite is a late Proterozoic metasedimentary upper crust.

On the other hand, the main Morozumi granite has a composition that is too Ca-rich to be derived from melting of common pelite-metagreywacke-volcaniclastic sources (Fig. 8a). Morozumi granites have Sr-Nd isotopic compositions that plot on the general trend linking mantle products and crustal magmatic rocks deriving from melting of different crustal levels, from deep granulite to upper crust metasediments (Di Vincenzo and Rocchi, 1999). Low $\varepsilon_{Nd(500\ Ma)}$ and moderately high $^{87}Sr/^{86}Sr_{(500\ Ma)}$ lead to prefer a granulite source. The cargo of relict zircons of the Morozumi granite is restricted to Grenvillian and mid-Neoproterozoic ages. Overall, the origin that can be envisaged for the main Morozumi granite is from melting of a Grenville-age deep crustal granulite, isotopically similar to the enderbites and metaenderbites from northern Victoria Land, which have $^{87}Sr/^{86}Sr_{(500\ Ma)}$=0.710 to 0.714 and $\varepsilon_{Nd(500\ Ma)}$= -7.8 to -

8.4, in turn geochemically similar to the Grenville-age Antarctic charnockites (Talarico et al., 1995).

The leucogranitic portions of the Morozumi dykes have Na-Ca-K relationships (Fig. 9) and Sr-Nd isotopic ratios (Fig. 7) potentially relating them to a source similar to that of the Morozumi granite. However, their higher silica content (Fig. 8a) and their field and geochemical relationships with host rocks suggest a different scenario (see further on).

7.3. Shallow processes: Origin of the diorite-granite trend

The rocks forming this trend (diorite, granodiorite, granite) display field evidence attesting for mingling-mixing relationships among them: dioritic melt did form pillows within the granite melt (Fig. 2n), and diffuse diorite-granite contacts are observed, with a granodiorite facies in between (Fig. 2h). Effective mixing was likely limited, as suggested by the minor volume of the granodiorite facies. Additionally, the granodiorite sometimes show angular blocks in sharp contact towards the host main granite, suggesting that the mingling process was limited, and rapidly evolved to more rigid behaviour. Chemical data (Fig. 5) and Sr-Nd isotopic systematics (Figs. 7 and 9) support field observations, with the granodiorite values fitting a simple mixing trend between the diorite and granite compositions.

7.4. Shallow processes: Origin of the tonalite-leucogranite trend

The Morozumi dykes metaluminous tonalites grade into evolved products in which white mica becomes a main mineral phase. This suggests a possible interaction with a peraluminous material. Potential candidates are both the Jupiter granite and the very minor aplite/leucogranites or the metasedimentary country rock. However, field evidence of stretched portions and streaks of mica-rich material incorporated from the host schist (Fig. 2f) into the subvertical eastern dykes suggests that the tonalite melt did engulf and stretch variable amounts of schist, leading to progressively silica-richer, more peraluminous compositions. Also in this case, field evidence is supported by Sr isotopic data (Fig. 9) indicating mixing relationships between the most primitive and the most evolved dykes. However, the lack of any evidence for thermal metamorphism in the host schist suggests that the interaction process was quick, with very limited heat transfer. Therefore, the term mixing is here used to describe the chemical result of the process, yet from the petrographic point of view the schist is just incorporated, stretched, dismembered and dispersed in the melt to the point that distiguishing the origin of single crystals is actually a hard, if possible, task.

8. Summary and implications

Field evidence, coupled with geochronological and petrographic-chemical-isotopic data outline a scenario of coeval emplacement of distinct melts issuing from different sources in the mantle and from different crustal levels as well (Fig. 10). These melts were interacting between them and/or with country rock during emplacement in a swiftly changing tectonic regime.

8.1. Magma origin and emplacement

Distinct magma sources were activated at almost the same time in the metasomatized mantle, in the upper crust, in the lower crust and in a domain where mantle and crust were mixed up by subduction erosion. The first magma emplaced in the Morozumi complex was a tonalite melt, intruded as subvertical dykes, parallel to the host schist foliation (Fig. 2a, d). The almost simultaneous emplacement of the main Morozumi granitic melt did generate a local compressional (flattening) regime with subhorizontal σ_1 leading to boudinage (Fig. 2g) of the vertically emplacing tonalite magma (Fig. 2a, d) which incorporated pieces of the host schists which were further stretched and dismembered into the crystallizing melt (Fig. 2f, g). The main intrusive body of the Morozumi granite was emplaced taking the shape of a subvertical large tabular body (Fig. 2a) with vertical magmatic foliation and lineation (Fig. 2b, l), in a transient stress regime ruled by the emplacement of main granitic melt. After that, the regional stress became dominant again, and further tonalite melt was thus intruded crosscutting the vertical foliation in a top-to-the-east thrusting regime evolving from ductile (melt present, Fig. 2l, o) to mylonitic (Fig. 2c, e). The emplacement regime of the peraluminous Jupiter granite can be inferred only from its intrusive relationships with the host schist, that indicate a brittle regime with shallowly dipping contacts (Fig. 2i), suggesting an overall tectonic regime finally coming to a rest.

Thus, four different melts were produced from the Morozumi lithospheric section in a short time span around 495 Ma (Fig. 10): (1) peraluminous granitic melts from the upper crust, (2) significant volumes of magma produced from recycling of Grenville-age, granulitic lower crust, (3) small volumes of tonalite melt deriving from subduction erosion-enriched mantle wedge, and (4) minor mafic melt from a metasomatized mantle. The contemporaneous activation of these four different sources is a remarkable example of the complexity of magma sources involved in a magmatic arc. Overall, it suggests that physical conditions for partial melting were attained contemporaneously in domains usually found at very different depths, and that produced melts found common pathways to emplace in the same site in the arc. In a subduction arc setting, such a scenario can occur when a relevant process of subduction erosion, possibly combined with underthrusting, bring into the sub-arc mantle large slices of upper and lower continental crust, and in the mantle wedge minor amounts of crustal material.

8.2. Geodynamic implications

Such a scenario fits well into the space-time geological setting of the Morozumi Range intrusive complex, which is located in the area facing the classical boundary between Wilson and Bowers terranes and was built up by the latest pulses of the Wilson magmatic arc, a few Ma after the docking of the Bowers arc-backarc system against the Wilson arc, which did occur a few km to the NE (Rocchi et al., 2011). The deeply underthrusted slices of continental crust and mafic material of the arc-backarc system reached ultra-high-pressure depths (Palmeri et al., 2011) and were soon exhumed, making it available in the mantle wedge and the overriding plate different sources such as metasomatized mantle, old lower crust and upper crust as well. Magma thus generated, rose and emplaced in the Morozumi Range in a NE-SW convergent tectonic regime, evolving to top-to-the NE midcrustal shearing (Rossetti et al., 2011) linked to the final docking from the NE of the Admiralty ribbon (Rocchi et al., 2011), also called Admiralty Block (Rossetti et al., 2011).

In a larger, orogen-scale view, this scenario leads to infer that the Antarctic margin of Gondwana in Victoria Land during Cambrian-Ordovician times was behaving in a differential way at different -current- latitudes. In the central Transantarctic Mountains, simple Sr-Nd isotope trends across the chain (Borg et al., 1990) indicate near-orthogonal subduction. Towards the north, in central Vicoria Land and southernmost northern Victoria Land, the margin behaved in a more complex way, with along-strike shifting of forearc slivers (Rocchi et al., 1998). In northernmost northern Victoria Land, multiple continental and oceanic arcs were active, and convergence was not a straightforward process, rather accretion did alternate with detachment of continental material-laden forearc-backarc from the main margin (Rocchi et al., 2011). In the southernmost sectors, a single subduction zone is invoked (Goodge et al., 2012), and a tectonic lock-up finally occurred at around 490 Ma, with production of postcollisional lamprophyres and granites emplaced in a brittle regime (Rocchi et al., 2009). Differently, the northern sector was characterized by a more complex geodynamic evolution, with alternating periods of single or double SW-verging active subduction zones, and contractional-accretionary stages alternated with extensional periods of the supra-subduction forearc

(Rocchi et al., 2011). In this framework, the classification of granites in syn- or post-tectonic becomes increasingly meaningless towards the north, where deformation occurred at several stages, until during the emplacement of very late intrusions, and even after that (Di Vincenzo et al., 2007), in absence of coeval magmatic activity.

Acknowledgements

This work has been carried out as part of the National Antarctic Research Program of Italy (PNRA, grant # Rocchi2004/4.6). The paper benefited of stimulating discussions with Claudio Ghezzo. The original manuscript received constructive criticisms by two anonymous reviewers as well as the Editor Nelson Eby, leading to significant improvement of the paper.

Tables

Table 1. Summary of field, petrographic and geochronological features of the lithologic units of the Morozumi Range intrusive complex..

Table 2. Major elements, trace elements and Sr-Nd isotopic data.

Table SM1. U-Pb LA-ICP-MS zircon data.

Figure Captions

Fig. 1. (a) Location map of the Transantarctic Mountains and Victoria Land in the frame of the early Paleozoic Ross-Delamerian orogen in Antarctica-Australia-Tasmania before the breakup of Gondwana (Foster et al., 2005; Glen, 2005). (b) Satellite view of Victoria Land, based on http://rapidfire.sci.gsfc.nasa.gov. For comparison between the representation of Victoria Land reported here (Rocchi et al., 2011) and that

reported in papers using the classical partition of northern Victoria Land into three terranes: (i) the Wilson terrane is here represented by the Wilson continental arc, (ii) the Bowers terrane is represented by the Bowers arc-backarc plus the southernmost part of the Tiger arc, and (iii) the Robertson Bay terrane is represented by the Admiralty crustal ribbon plus the northernmost part of the Tiger arc. IG: “postcollisional” granites and felsic dykes; VL: "postcollisional” lamprophyric dykes (Rocchi et al., 2009). (c) Magnification of the Morozumi Range, with location of field photographs reported in Figure 2.

Fig. 2. Field photographs of the Morozumi Range intrusive complex. (a) Panoramic view from NE of the northern Morozumi Range, vertical relief 1300 m, horizontal view ca. 10 km. Dark rocks: Morozumi phyllites; light rocks: Morozumi granite. (b) Morozumi granite, width of viewfield 40 cm. (c) Morozumi crestal dyke intruding Morozumi granite with a top-to-the-east shear band at the lower contact. (d) Morozumi Range, view from NW: Morozumi granite on the right (west), Morozumi phyllites to the left (east) intruded by Morozumi eastern dykes. (e) Detail of (c): top-to-the-east shear band at the contact between Morozumi crestal dyke (above) intruding Morozumi granite (below). (f) Streaks of stretched Morozumi phyllites into Morozumi eastern dyke; person for scale. (g) Stretched portions of eastern dykes (light colour), with asymmetric boudinage structures, intruded into Morozumi phyllites (dark); hammer for scale. (h) Detail of (m): diffuse contact between Morozumi diorite, granodiorite and granite; hammers for scale. (i) Jupiter granite, light-coloured, intruding Morozumi phyllites with subhorizontal contact at Jupiter Amphitheatre; vertical relief 300 m. (l) Western dyke, below, intruding Morozumi granite; person for scale. (m) Dykes and stocks of Morozumi diorite intruding Morozumi granite; persons for scale. (n) Detail of (m): pillows of Morozumi diorite into a felsic facies of Morozumi granite at the diorite-granite contact; hammer for scale. (o) Detail of (l): western dyke (below), intruding vertically foliated Morozumi granite and aplite as well; hammer for scale.

Fig. 3. $^{206}Pb/^{238}U$ vs $^{207}Pb/^{235}U$ concordia plots for concordant ages with a 2σ error. Plots and concordia ages obtained by Isoplot software (Ludwig, 2012). Representative SEM-CL images are reported.

Fig. 4. Cumulative probability distribution (Ludwig, 2012) of $^{206}Pb/^{238}U$ ages for the Morozumi intrusive units and host rocks. Representative SEM-CL images are reported.

Fig. 5. Total Alkali-Silica (TAS) diagram of the Morozumi intrusive units. Also reported for comparison: (i) intrusive rocks emplaced at 490-500 Ma in the Wilson arc: (i) Abbott gabbro, Confusion tonalites, Abbott granites, Vegetation leucogranites (Di Vincenzo and Rocchi, 1999; Rocchi et al., 2004), Vegetation lamprophyres and Irizar granites-dykes (Rocchi et al., 2009), and (ii) intrusive rocks emplaced earlier in the Tiger oceanic arc, i.e. Tiger gabbro (Bracciali et al., 2009).

Fig. 6. N-MORB-normalized plots (Sun and McDonough, 1989) of incompatible elements. (a) Morozumi diorite samples, compared to the Abbott gabbro (Di Vincenzo and Rocchi, 1999), the Vegetation lamprophyres from central Victoria Land (Rocchi et al., 2009) and the Tiger gabbro from the Tiger magmatic arc (Fig. 1) (Bracciali et al., 2009). (b) Morozumi tonalite dyke, compared to the Confusion tonalite (Di Vincenzo and Rocchi, 1999; Rocchi et al., 2004) and the Tiger gabbro from the Tiger magmatic arc (Fig. 1) (Bracciali et al., 2009).

Fig. 7. $\varepsilon_{Nd\ (500\ Ma)}$ vs $^{87}Sr/^{86}Sr_{(500\ Ma)}$ plot of the Morozumi mafic-intermediate intrusive rocks. Also reported for comparison: (i) intrusive complexes emplaced at around 490-500 Ma in the Wilson arc: (i) the Abbott gabbro and its hybridization trend with melts from the deep crust, the Confusion tonalites, Vegetation leucogranites and their hybridization trend with melts from mesedimentary upper crust (Di Vincenzo and Rocchi, 1999; Rocchi et al., 2004), (ii) the Irizar granites and dykes (Rocchi et al., 2009), and (iii) intrusive rocks emplaced earlier in the Tiger oceanic arc, i.e. Tiger gabbro (Bracciali et al., 2009).

Fig. 8. (a) Ternary diagrams showing Na-K-Ca relationships for the rocks of the Morozumi intrusive complex compared to pelite-, greywacke- and metavolcanoclastics-derived fluid-absent experimental melts (Montel and Vielzeuf, 1997; Patiño Douce and Beard, 1996; Patiño Douce and Johnston, 1991; Sisson et al., 2005; Skjerlie and Johnston, 1996; Stevens et al., 1997; Vielzeuf and Holloway, 1988) and to adakite and TTG fields and evolutionary trends (Defant and Drummond, 1993). (b) Classical Sr/Y vs. Sr plot comparing the Morozumi mafic-intermediate intrusive rocks with the adakite and andesite-dacite-rhyolite (ADR) fields (Defant and Drummond, 1993)

Fig. 9. $^{87}Sr/^{86}Sr$ vs. 1000/Sr plot, showing mixing trends as linear paths.

Fig. 10. Idealized sketch of the reconstructed scenario from the emplacement level down to source depth.

References

Adams, C.J., Bradshaw, J.D., Ireland, T.R., 2013. Provenance connections between late Neoproterozoic and early Palaeozoic sedimentary basins of the Ross Sea region, Antarctica, south-east Australia and southern Zealandia. Antarctic Science 26, 173-182.

Alagna, K.E., Petrelli, M., Perugini, D., Poli, G., 2008. Micro-Analytical Zircon and Monazite U-Pb Isotope Dating by Laser Ablation-Inductively Coupled Plasma-Quadrupole Mass Spectrometry. Geostandards and Geoanalytical Research 32, 103-120.

Allibone, A., Wysoczanski, R., 2002. Initiation of magmatism during the Cambro-Ordovician Ross orogeny in southern Victoria Land, Antarctica. Geological Society of America Bulletin 114, 1007-1018.

Boger, S.D., Miller, J.M., 2004. Terminal suturing of Gondwana and the onset of the Ross-Delamerian Orogeny: the cause and effect of an Early Cambrian reconfiguration of plate motions. Earth and Planetary Science Letters 219, 35-48.

Bomparola, R.M., Ghezzo, C., Belousova, E., Griffin, W.L., O'Reilly, S.Y., 2007. Resetting of the U-Pb zircon system in Cambro-Ordovician intrusives of the Deep Freeze Range, northern Victoria Land, Antarctica. Journal of Petrology 48, 327-364.

Borg, S.G., DePaolo, D.J., Smith, B.M., 1990. Isotopic structure and tectonics of the Central Tansantarctic Mountains. Journal of Geophysical Research 95, 6647-6667.

Bracciali, L., Di Vincenzo, G., Rocchi, S., Ghezzo, C., 2009. The Tiger Gabbro from northern Victoria Land, Antarctica: the roots of an island arc within the early Palaeozoic margin of Gondwana. Journal of the Geological Society, London 166, 711-724.

Bradshaw, J.D., Weaver, S.D., Laird, M.G., 1985. Suspect Terranes and Cambrian Tectonics in Northern Victoria Land, Antarctica, in: Howell, D.G. (Ed.), Tectonostratigraphic

Terranes of the Circum-Pacific Region, Circum-Pacific Conference for Energy and Mineral Resources, Earth Science Series, pp. 467-479.

Brown, M., 2013. Granite: From genesis to emplacement. Geological Society of America Bulletin 125, 1079-1113.

Brun, J.-P., Faccenna, C., 2008. Exhumation of high-pressure rocks driven by slab rollback. Earth and Planetary Science Letters 272, 1-7.

Castillo, P.R., 2012. Adakite petrogenesis. Lithos 134–135, 304-316.

Cawood, P.A., 2005. Terra Australis Orogen: Rodinia breakup and development of the Pacific and Iapetus margins of Gondwana during the Neoproterozoic and Paleozoic. Earth Science Reviews 69, 249-279.

Crispini, L., Di Vincenzo, G., Palmeri, R., 2007. Petrology and $^{40}Ar–^{39}Ar$ dating of shear zones in the Lanterman Range (northern Victoria Land, Antarctica): implications for metamorphic and temporal evolution at terrane boundaries. Mineralogy and Petrology 89, 217-249.

Davidson, J.P., Hora, J.M., Garrison, J.M., Dungan, M.A., 2005. Crustal forensics in arc magmas. Journal of Volcanology and Geothermal Research 140, 157-170.

Defant, M.J., Drummond, M.S., 1990. Derivation of some modern arc magmas by melting of young subducted lithosphere. Nature 347, 662-665.

Defant, M.J., Drummond, M.S., 1993. Mount St. Helens: potential example of the partial melting of the subducted lithosphere in a volcanic arc. Geology 21, 541–550. Geology 21, 547-550.

DePaolo, D.J., 1981. Trace element and isotopic effects of combined wallrock assimilation and fractional crystallisation. Earth and Planetary Science Letters 53, 189-202.

Di Vincenzo, G., Carosi, R., Palmeri, R., Tiepolo, M., 2007. A comparative U–Th–Pb (zircon–monazite) and $^{40}Ar–^{39}Ar$ (muscovite–biotite) study of shear zones in northern Victoria Land (Antarctica): implications for geochronology and localized reworking of the Ross Orogen. Journal of Metamorphic Geology 25, 605-630.

Di Vincenzo, G., Grande, a., Rossetti, F., 2014. **Paleozoic siliciclastic rocks from northern Victoria Land (Antarctica): Provenance, timing of deformation, and implications for the Antarctica-Australia connection**. Geological Society of America Bulletin 126, 1416-1438.

Di Vincenzo, G., Rocchi, S., 1999. Origin and interaction of mafic and felsic magmas in an evolving late orogenic setting: the early Paleozoic Terra Nova Intrusive Complex, Antarctica. Contributions to Mineralogy and Petrology 137, 15-35.

Encarnación, J., Grunow, A., 1996. Changing magmatic and tectonic style along the paleo-Pacific margin of Gondwana and the onset of early Paleozoic magmatism in Antarctica. Tectonics 15, 1325-1341.

Farina, F., Dini, A., Rocchi, S., Stevens, G., 2014. Extreme mineral-scale Sr isotope heterogeneity in granites by disequilibrium melting of the crust. Earth and Planetary Science Letters 399, 103-115.

Farina, F., Stevens, G., 2011. Source controlled 87Sr/86Sr isotope variability in granitic magmas: The inevitable consequence of mineral-scale isotopic disequilibrium in the protolith. Lithos 122, 189-200.

Federico, L., Capponi, G., Crispini, L., 2006. The Ross orogeny of the transantarctic mountains: a northern Victoria Land perspective. International Journal of Earth Sciences 95, 759-770.

Ferraccioli, F., Armadillo, E., Zunino, A., Bozzo, E., Rocchi, S., Armienti, P., 2009. Magmatic and tectonic patterns over the Northern Victoria Land sector of the Transantarctic Mountains from new aeromagnetic imaging. Tectonophysics 478, 43-61.

Ferraccioli, F., Bozzo, E., Capponi, G., 2002. Aeromagnetic and gravity anomaly constraints for an early Paleozoic subduction system of Victoria Land, Antarctica. Geophysical Research Letters 29, 10.1029/20012001GLO20014138.

Finn, C., Moore, D., Damaske, D., Mackey, T., 1999. Aeromagnetic legacy of early subduction along the Pacific margin of Gondwana. Geology 27, 1087-1090.

Flöttmann, T., Gibson, G.M., Kleinschmidt, G., 1993. Structural continuity of the Ross and Delamerian orogens of Antarctica and Australia along the margin of the paleo-Pacific. Geology 21, 319-322.

Foden, J., Elburg, M.A., Dougherty-Page, J., Burtt, A., 2006. The timing and duration of the Delamerian Orogeny: correlation with the Ross Orogen and implications for Gondwana assembly. Journal of Geology 114, 189-210.

Foster, D.A., Grey, D.R., Spaggiari, C., 2005. Timing of subduction and exhumation along the Cambrian East Gondwana margin, and the formation of Paleozoic backarc basins. Geological Society of America Bulletin 117, 105-116.

GANOVEX TEAM, 1987. Geological Map of North Victoria Land, Antarctica, 1:500,000 - Explanatory notes -. Geologisches Jahrbuch B66, 7-79.

Gemelli, M., Rocchi, S., Di Vincenzo, G., Petrelli, M., 2009. Accretion of juvenile crust at the Early Palaeozoic Antarctic margin of Gondwana: geochemical and geochronological evidence from granulite xenoliths. Terra Nova 21, 151-191.

Giacomini, F., Tiepolo, M., Dallai, L., Ghezzo, C., 2007. On the onset and evolution of the Ross-orogeny magmatism in North Victoria Land - Antarctica. Chemical Geology 240, 103-128.

Gibson, G.M., Ireland, T.R., 1996. Extension of Delamerian (Ross) orogen into western New Zealand: Evidence from zircon ages and implications for crustal growth along the Pacific margin of Gondwana. Geology 24, 1087-1090.

Gibson, G.M., Morse, M.P., Ireland, T.R., Nayak, G.K., 2011. Arc-continent collision and orogenesis in western Tasmanides: Insights from reactivated basement structures and formation of an ocean-continent transform boundary off western Tasmania. Gondwana Research 19, 608-627.

Gibson, G.M., Wright, T.O., 1985. Importance of thrust faulting in the tectonic development of northern Victoria Land, Antarctica. Nature 315, 480-483.

Glen, R.A., 2005. The Tasmanides of eastern Australia, in: Vaughan, A.P.M., Leat, P.M., Pankhurst, R.J. (Eds.), Terrane processes at the margins of Gondwana. Geological Society Special Publications, 246, London, pp. 23-96.

Glen, R.A., 2013. Refining accretionary orogen models for the Tasmanides of eastern Australia. Australian Journal of Earth Sciences 60, 315-370.

Glen, R.A., Meffre, S., Scott, R.J., 2007. Benambran Orogeny in the Eastern Lachlan Orogen, Australia. Australian Journal of Earth Sciences: An International Geoscience Journal of the Geological Society of Australia 54, 385 - 415.

Goodge, J.W., 2002. From Rodinia to Gondwana: supercontinent evolution in the Transantarctic Mountains, in: Gamble, J.A., Skinner, D.N.B., Henrys, S. (Eds.), Proceedings of the 8th International Symposium on Antarctic Earth Sciences, Royal Society of New Zealand Bulletin, pp. 61-74.

Goodge, J.W., Fanning, C.M., Norman, M.D., Bennett, V.C., 2012. Temporal, Isotopic and Spatial Relations of Early Paleozoic Gondwana-Margin Arc Magmatism, Central Transantarctic Mountains, Antarctica. Journal of Petrology 53, 2027-2065.

Goodge, J.W., Williams, I.S., Myrow, P., 2004. Provenance of Neoproterozoic and lower Paleozoic siliciclastic rocks of the central Ross orogen, Antarctica: Detrital record of rift-, passive-, and active-margin sedimentation. Geological Society of America Bulletin 116, 1253-1279.

Hacker, B.R., Kelemen, P.B., Behn, M.D., 2011. Differentiation of the continental crust by relamination. Earth and Planetary Science Letters 307, 501-516.

Harris, N., Ayres, M., 1998. The implications of Sr-isotope disequilibrium for rates of prograde metamorphism and melt extraction in anatectic terrains, in: Treloar, P.J., O'Brien, P.J. (Eds.), What drives metamorphism and metamorphic reactions? Geological Society, London, Special Publication, pp. 171-182.

Kay, S.M., Godoy, E., Kurtz, A., 2005. Episodic arc migration, crustal thickening, subduction erosion, and magmatism in the south-central Andes. Geological Society of America Bulletin 117, 67-88.

Kleinschmidt, G., Tessensohn, F., 1987. Early Paleozoic westward directed subduction at the Pacific continental margin of Antarctica, Sixth Gondwana Symposium. American Geophysical Union, Geophysical Monograph, 40, pp. 89-105.

Ludwig, K.R., 2012. Isoplot/Ex 3.75, 3.00 ed. Berkeley Geochronology Center, Special Publication No. 4.

Montel, J.-M., Vielzeuf, D., 1997. Partial melting of metagreywackes, Part II. Compositions of minerals and melts. Contributions to Mineralogy and Petrology 128, 176-196.

O'Hara, M.J., 1977. Geochemical evolution during fractional crystallisation of a periodically refilled magma chamber. Nature 266, 503-507.

Palmeri, R., Talarico, F.M., Ricci, C.A., 2011. Ultrahigh-pressure metamorphism at the Lanterman Range (northern Victoria Land, Antarctica). Geological Journal 46, 126-136.

Patiño Douce, A.E., Beard, J.S., 1996. Effect of P, f(O2) and Mg/Fe ratio on dehydration melting of model metagreywackes. Journal of Petrology 37, 999-1024.

Patiño Douce, A.E., Johnston, A.D., 1991. Phase equilibria and melt productivity in the pelitic system: implications for the origin of peraluminous granitoids and aluminous granulites. Contributions to Mineralogy and Petrology 107, 202-218.

Pearce, J.A., Peate, D.W., 1995. Tectonic implications of the composition of volcanic arc magmas. Annual Revue of Earth and Planetary Sciences 23, 251-285.

Rocchi, S., Armienti, P., D'Orazio, M., Tonarini, S., Wijbrans, J., Di Vincenzo, G., 2002. Cenozoic magmatism in the western Ross Embayment: role of mantle plume vs. plate dynamics in the development of the West Antarctic Rift System. Journal of Geophysical Research 107, 2195.

Rocchi, S., Bracciali, L., Di Vincenzo, G., Gemelli, M., Ghezzo, C., 2011. Arc accretion to the early Paleozoic Antarctic margin of Gondwana in Victoria Land. Gondwana Research 19, 594-607.

Rocchi, S., Capponi, G., Crispini, L., Di Vincenzo, G., Ghezzo, C., Meccheri, M., Palmeri, R., 2003. Mafic rocks at the Wilson-Bowers terrane transition and within the Bowers terrane: implications for a geodynamic model of the Ross Orogeny. Terra Antartica Reports 9, 145-148.

Rocchi, S., Di Vincenzo, G., Ghezzo, C., 2004. The Terra Nova Intrusive Complex (Victoria Land, Antarctica), with 1:50,000 Geopetrographic Map. Terra Antartica Reports 10, 51.

Rocchi, S., Di Vincenzo, G., Ghezzo, C., Nardini, I., 2009. Granite-lamprophyre connection in the latest stages of the Early Paleozoic Ross Orogeny (Victoria Land, Antarctica). Geological Society of America Bulletin 121, 801-819.

Rocchi, S., Tonarini, S., Armienti, P., Innocenti, F., Manetti, P., 1998. Geochemical and isotopic structure of the early Palaeozoic active margin of Gondwana in northern Victoria Land, Antarctica. Tectonophysics 284, 261-281.

Roland, N.W., Läufer, A., Rossetti, F., 2004. Revision of the terrane model of northern Victoria Land. Terra Antartica 11, 55-65.

Rossetti, F., Storti, F., Busetti, M., Di Vincenzo, G., Lisker, F., Rocchi, S., Salvini, F., 2006a. Eocene initiation of Ross Sea dextral faulting and implications for East Antarctic neotectonics. Journal of the Geological Society, London 163, 119-126.

Rossetti, F., Tecce, F., Aldega, L., Brilli, M., Faccenna, C., 2006b. Deformation and fluid flow during orogeny at the palaeo- active margin of Gondwana: the Early Palaeozoic Robertson accretionary complex (north Victoria Land, Antarctica). Journal of Metamorphic Geology 24, 33-53.

Rossetti, F., Vignaroli, G., Di Vincenzo, G., Gerdes, A., Ghezzo, C., Theye, T., Balsamo, F., 2011. Long-lived orogenic construction along the paleo-Pacific margin of Gondwana (Deep Freeze Range, North Victoria Land, Antarctica). Tectonics 30, TC4008.

Rushmer, T., 1991. Partial melting of two amphibolites: contrasting experimental results under fluid-absent conditions. Contributions to Mineralogy and Petrology 107, 41-59.

Sisson, T.W., Ratajeski, K., Hankins, W.B., Glazner, A.F., 2005. Voluminous granitic magmas from common basaltic sources. Contributions to Mineralogy and Petrology 148, 635–661.

Skjerlie, K.P., Johnston, A.D., 1996. Vapour-absent melting from 10 to 20 kbar of crustal rocks that contain multiple hydrous phases: implications for anatexis in the deep to very deep continental crust and active continental margins. Journal of Petrology 37, 661-691.

Stevens, G., Clemens, J.D., Droop, G.T.R., 1997. Melt production during granulite-facies anatexis: experimental data from “primitive” metasedimentary protoliths. Contributions to Mineralogy and Petrology 128, 352-370.

Stump, E., 1995. The Ross Orogen of the Transantarctic Mountains. Cambridge University Press, Cambridge.

Stump, E., Gootee, B., Talarico, F., 2006. Tectonic model for development of the Byrd Glacier Discontinuity and surrounding regions of the Transantarctic Mountains during the Neoproterozoic - Early Paleozoic, in: Fütterer, D.K., Damaske, D., Kleinschmidt, G., Miller, H., Tessensohn, F. (Eds.), Antarctica – Contributions to Global Earth Sciences, Proceedings of the IX International Symposium of Antarctic Earth Sciences, Potsdam, 2003. Springer-Verlag, Berlin Heidelberg New York, pp. 181-190.

Stump, E., Laird, M.G., Bradshaw, J.D., Holloway, J.R., Borg, S.G., Lapham, K.E., 1983. Bowers graben and associated tectonic features cross northern Victoria Land, Antarctica. Nature 304, 334-336.

Stump, E., White, A.J.R., Borg, S.G., 1986. Reconstruction of Australia and Antarctica: evidence from granites and recent mapping. Earth and Planetary Science Letters 79, 348-360.

Sun, S.S., McDonough, W.F., 1989. Chemical and isotopic systematics of oceanic basalts: implications for mantle composition and processes, in: Saunders, A.D., Norry, M.J. (Eds.), Magmatism in the Ocean Basins. Geological Society of London Special Publication, pp. 313-345.

Talarico, F., Borsi, L., Lombardo, B., 1995. Relict granulites of the Ross Orogen of northern Victoria Land (Antarctica). II - Geochemistry and paleo-tectonic implications. Precambrian Research 75, 157-174.

Tamponi, M., Bertoli, F., Innocenti, F., Leoni, L., 2003. X-ray fluorescence analysis of major elements in silicate rocks using fused glass discs. Atti della Società Toscana di Scienze Naturali, Memorie Serie A 107, 73-80.

Tessensohn, F., Henjes-Kunst, F., 2005. Northern Victoria Land terranes, Antarctica: far travelled or local products?, in: Vaughan, A.P.M., Leat, P., Pankhurst, R.J. (Eds.), Terrane processe at the margin of Gondwana. Geological Society, London, Special Publications, 246, pp. 275-291.

Turner, S., Haines, P., Foster, D., Powell, R., Sandiford, M., Offler, R., 2009. Did the Delamerian Orogeny Start in the Neoproterozoic? The Journal of Geology 117, 575-583.

Vielzeuf, D., Holloway, J.R., 1988. Experimental determination of the fluid-absent melting relations in the pelitic system. Consequences for crustal differentiation. Contributions to Mineralogy and Petrology 98, 257-276.

von Huene, R., Ranero, C.R., Vannucchi, P., 2004. Generic model of subduction erosion. Geology 32, 913-916.

Weaver, S.D., Bradshaw, J.D., Laird, M.G., 1984. Geochemistry of Cambrian volcanics of the Bowers Supergroup and implication for early Paleozoic tectonic evolution of Northern Victoria Land Antarctica. Earth and Planetary Science Letters 68, 128-140.

Wilson, M., 1989. Igneous Petrogenesis. Unwin Hyman, London.

Figure 1
Click here to download high resolution image

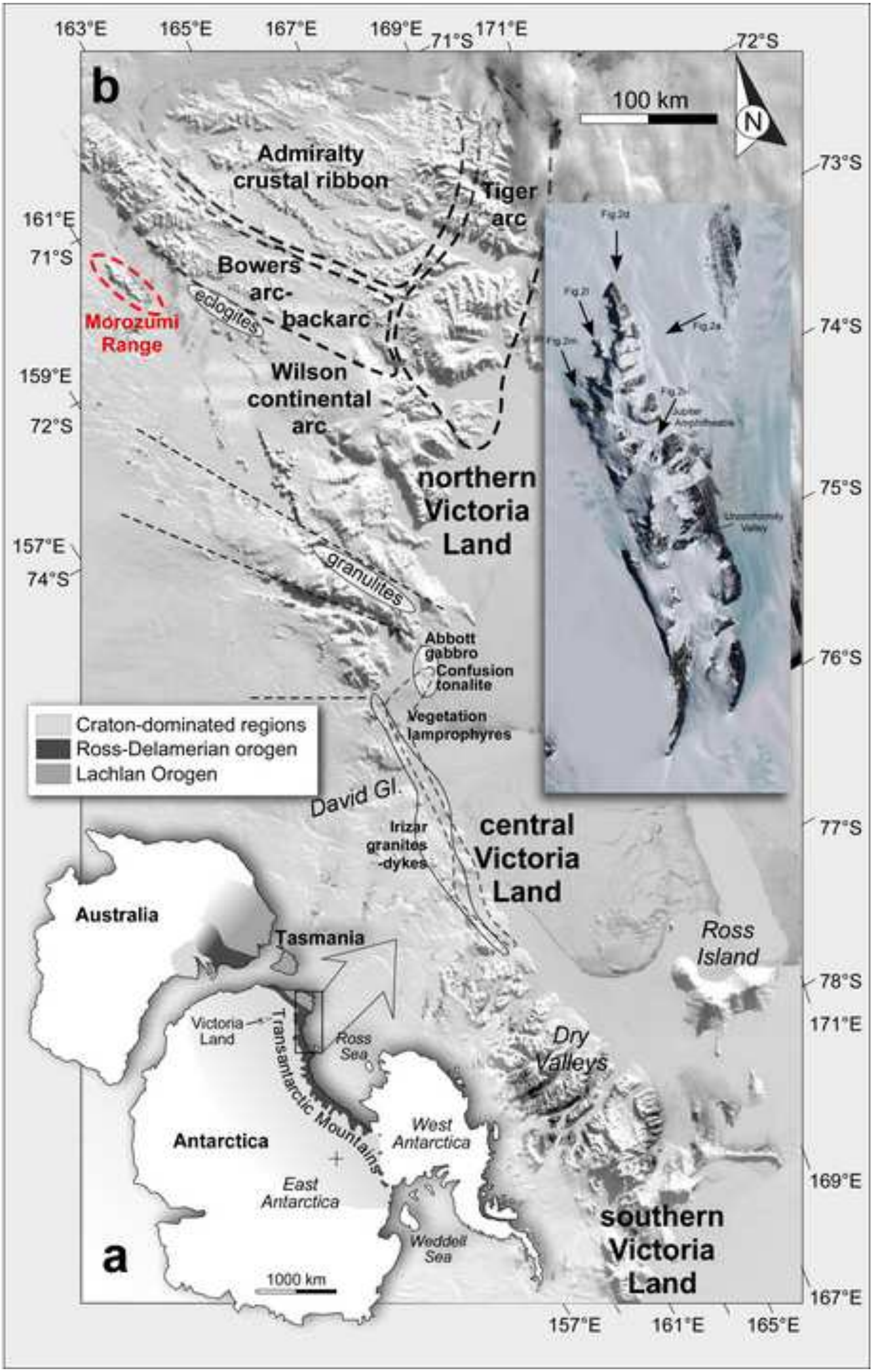

Figure 2

Click here to download high resolution image

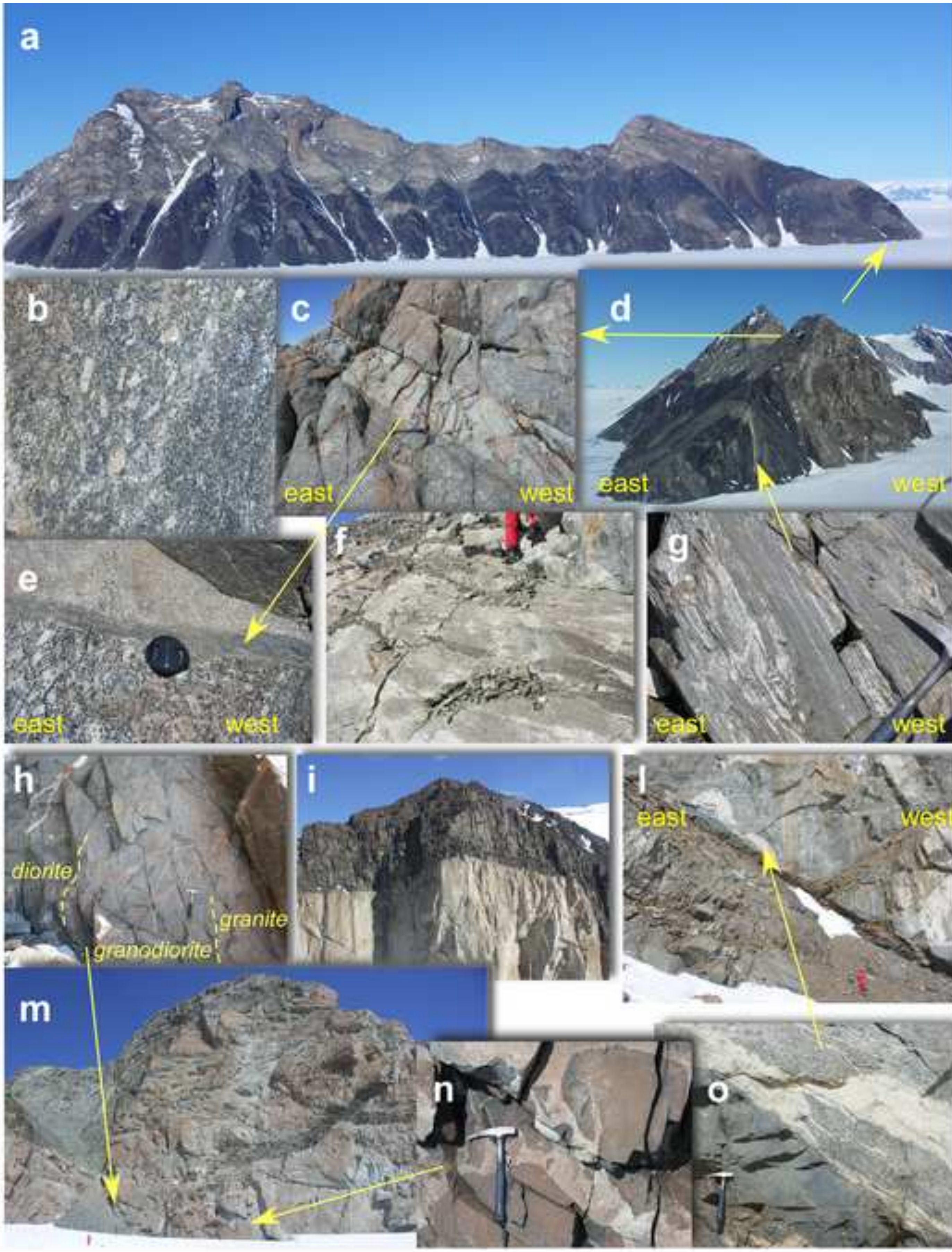

Figure 3

Click here to download high resolution image

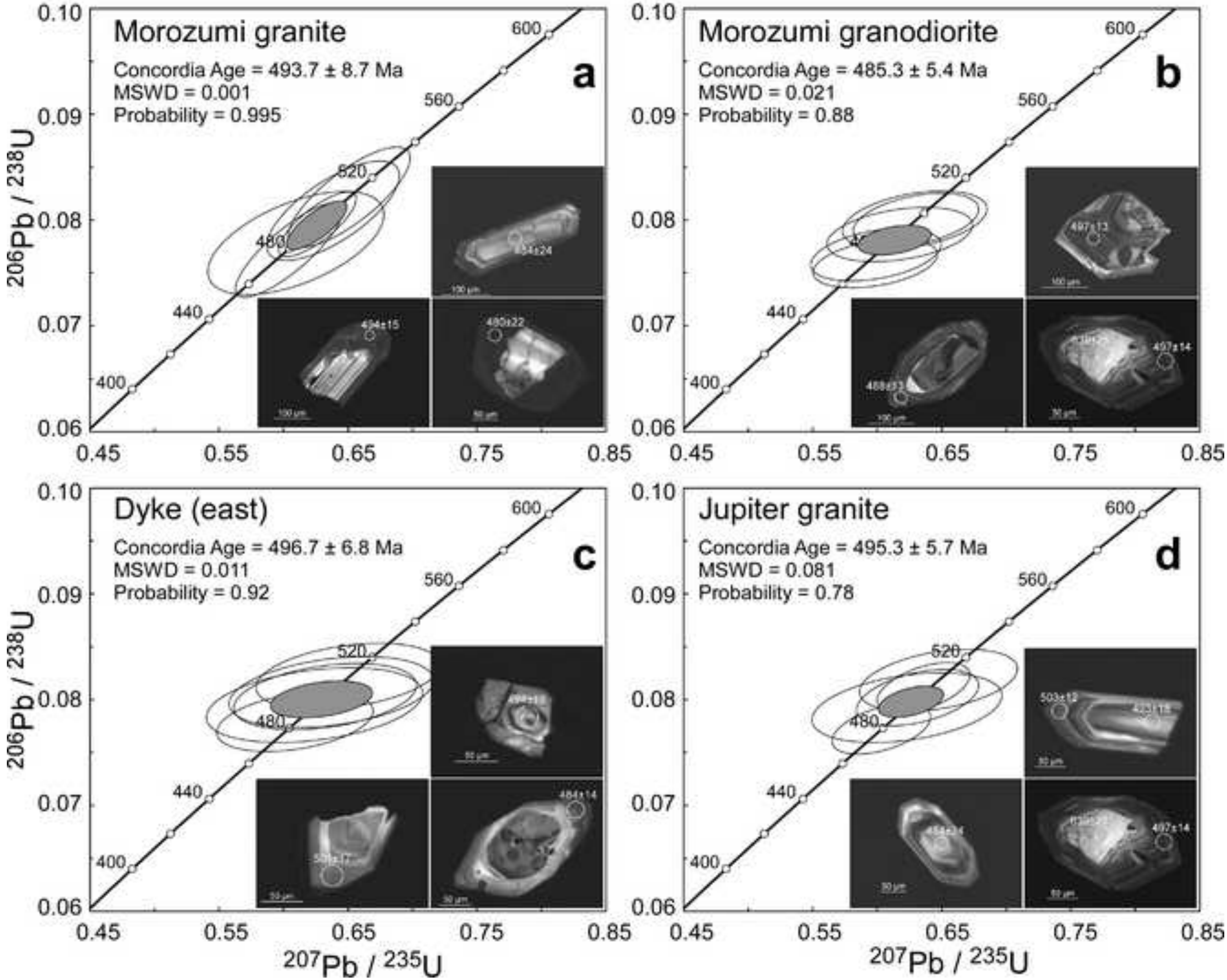

Figure 4
Click here to download high resolution image

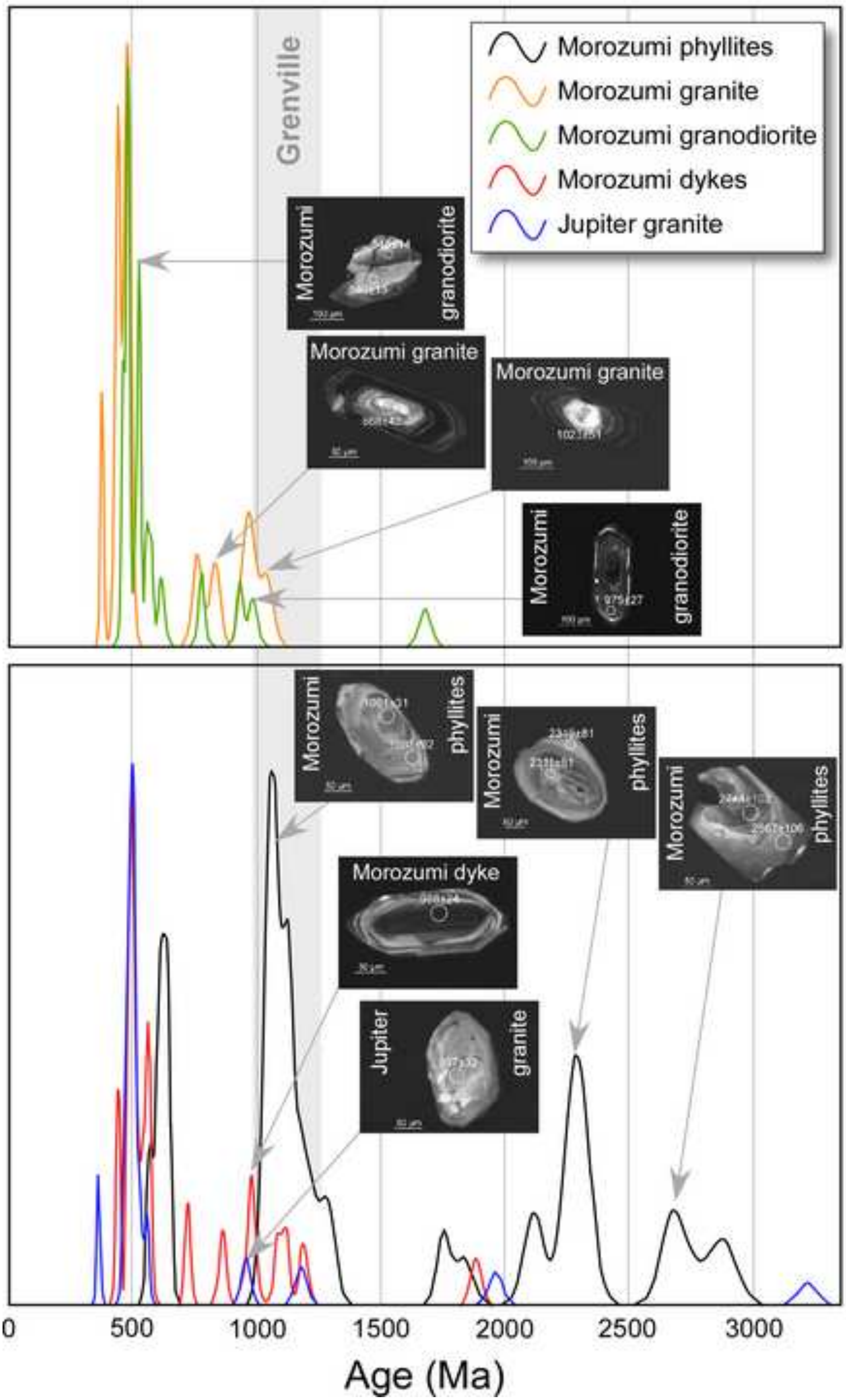

Figure 5
Click here to download high resolution image

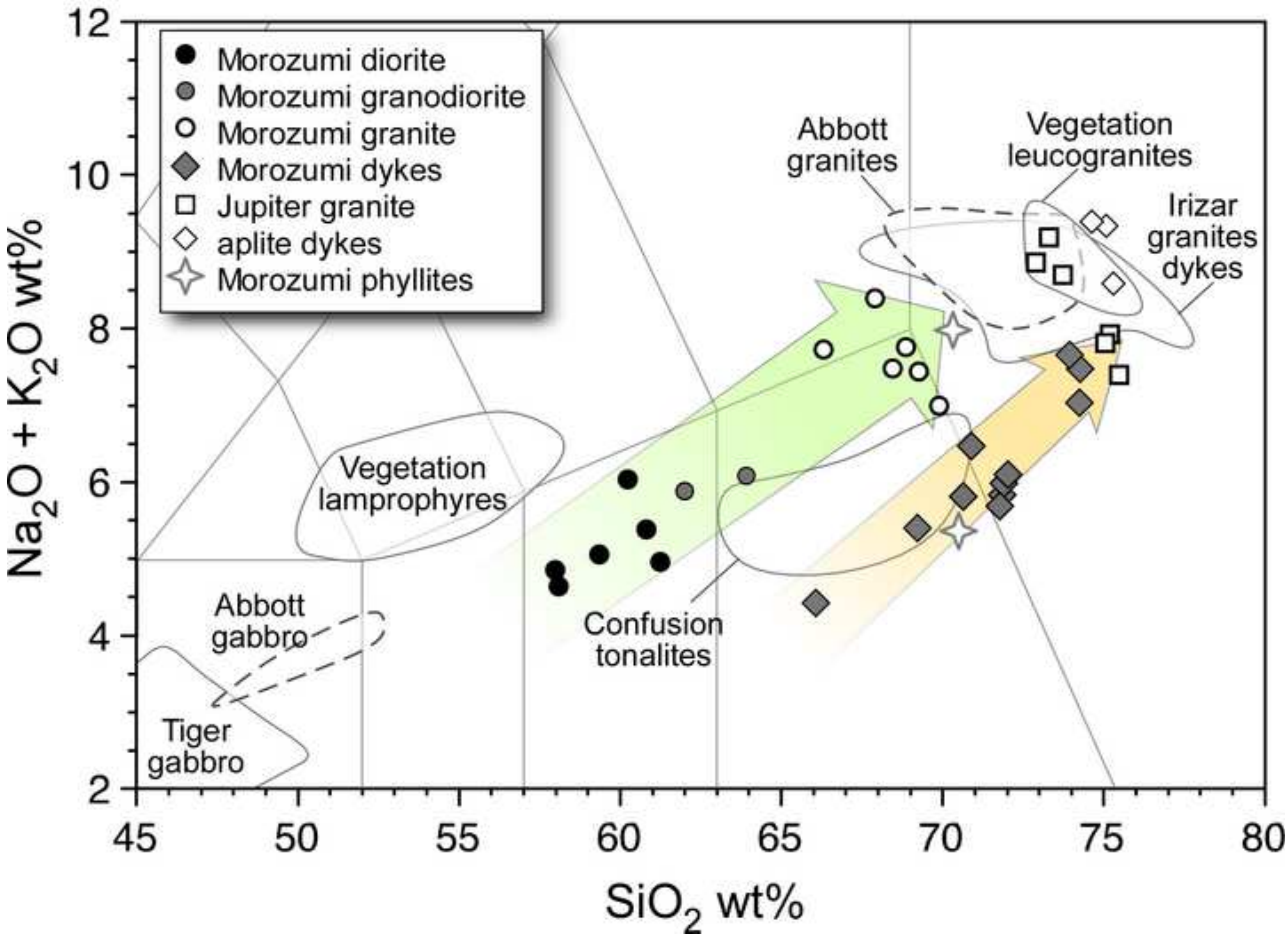

Figure 6
Click here to download high resolution image

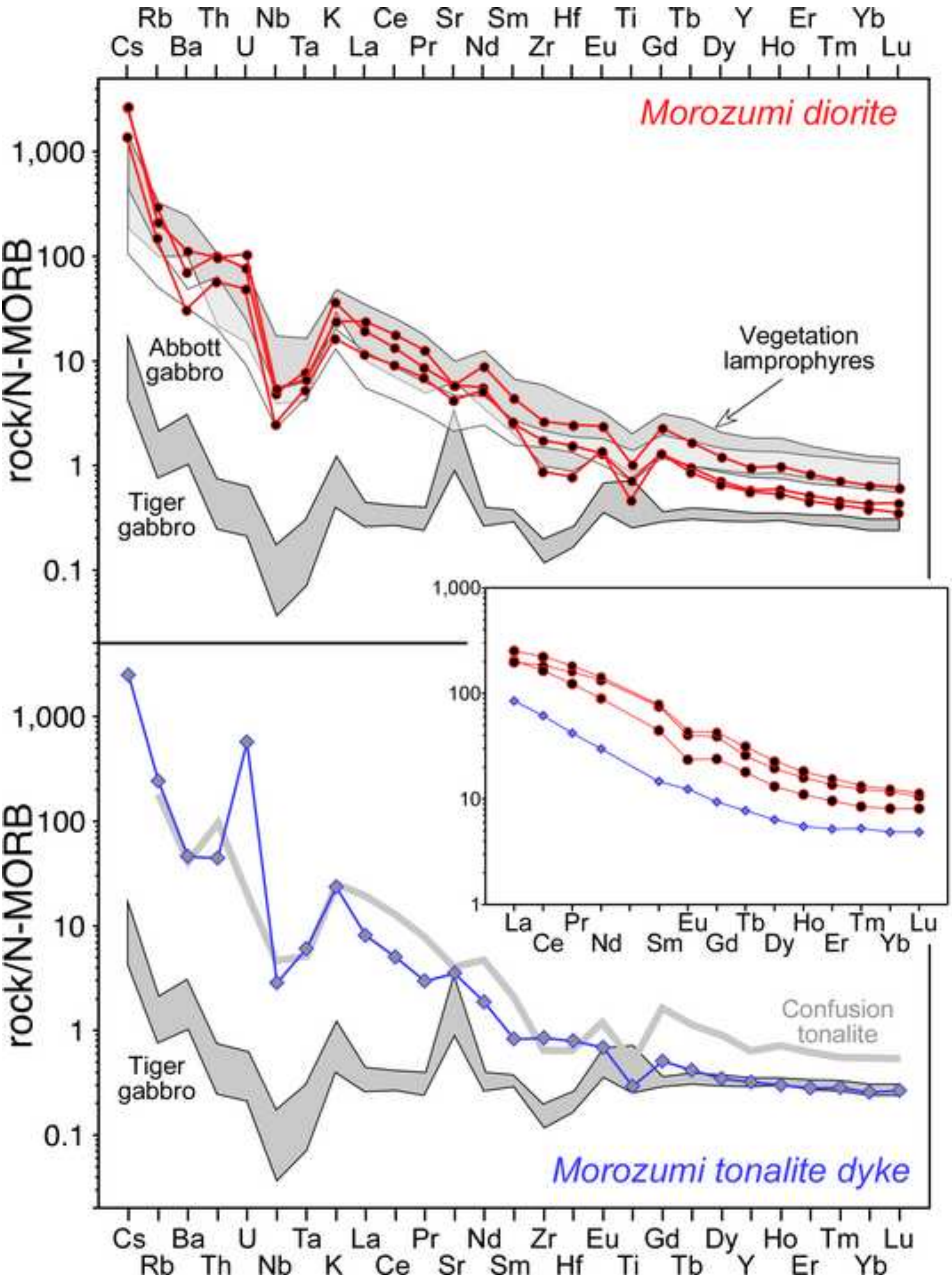

Figure 7
Click here to download high resolution image

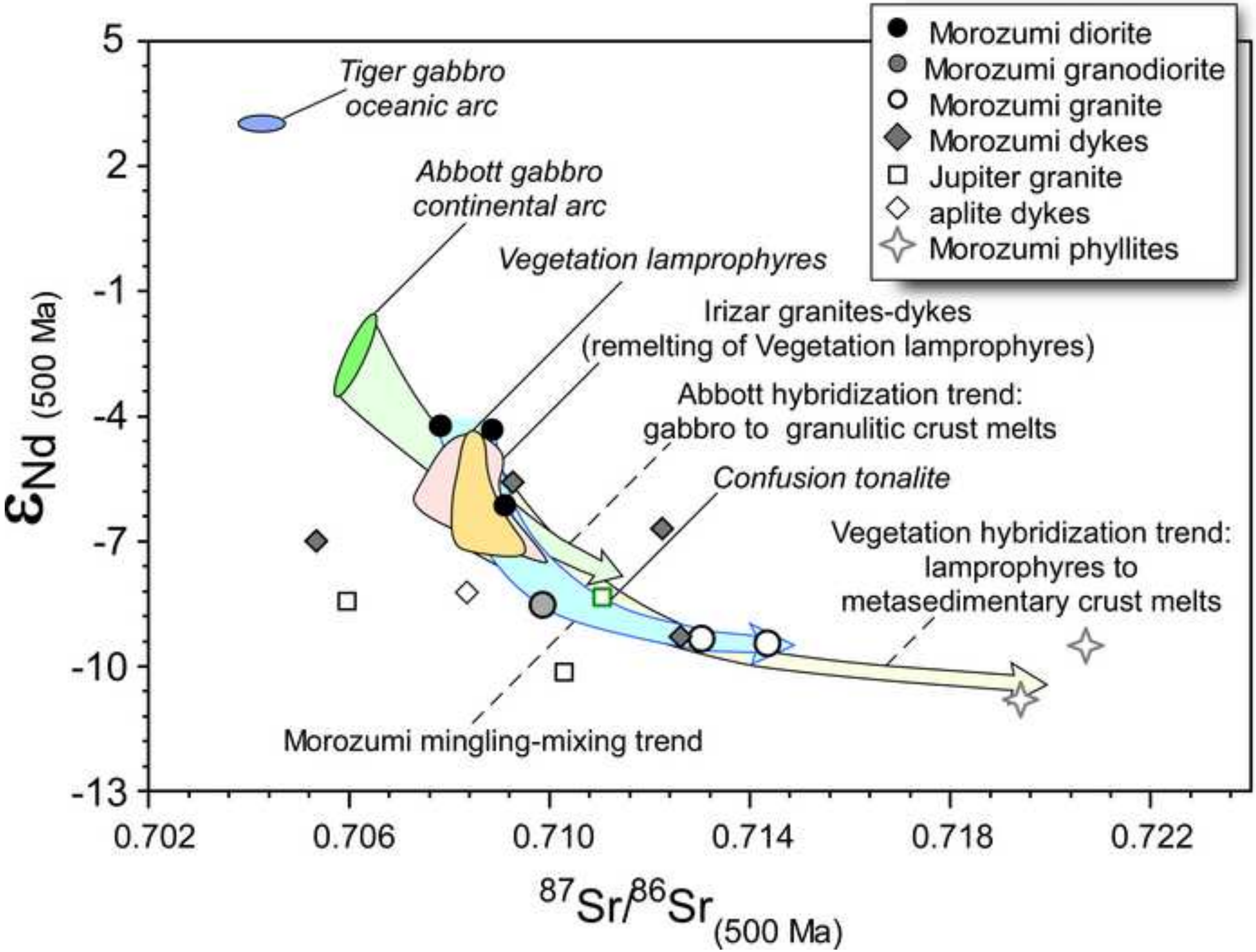

Figure 8
Click here to download high resolution image

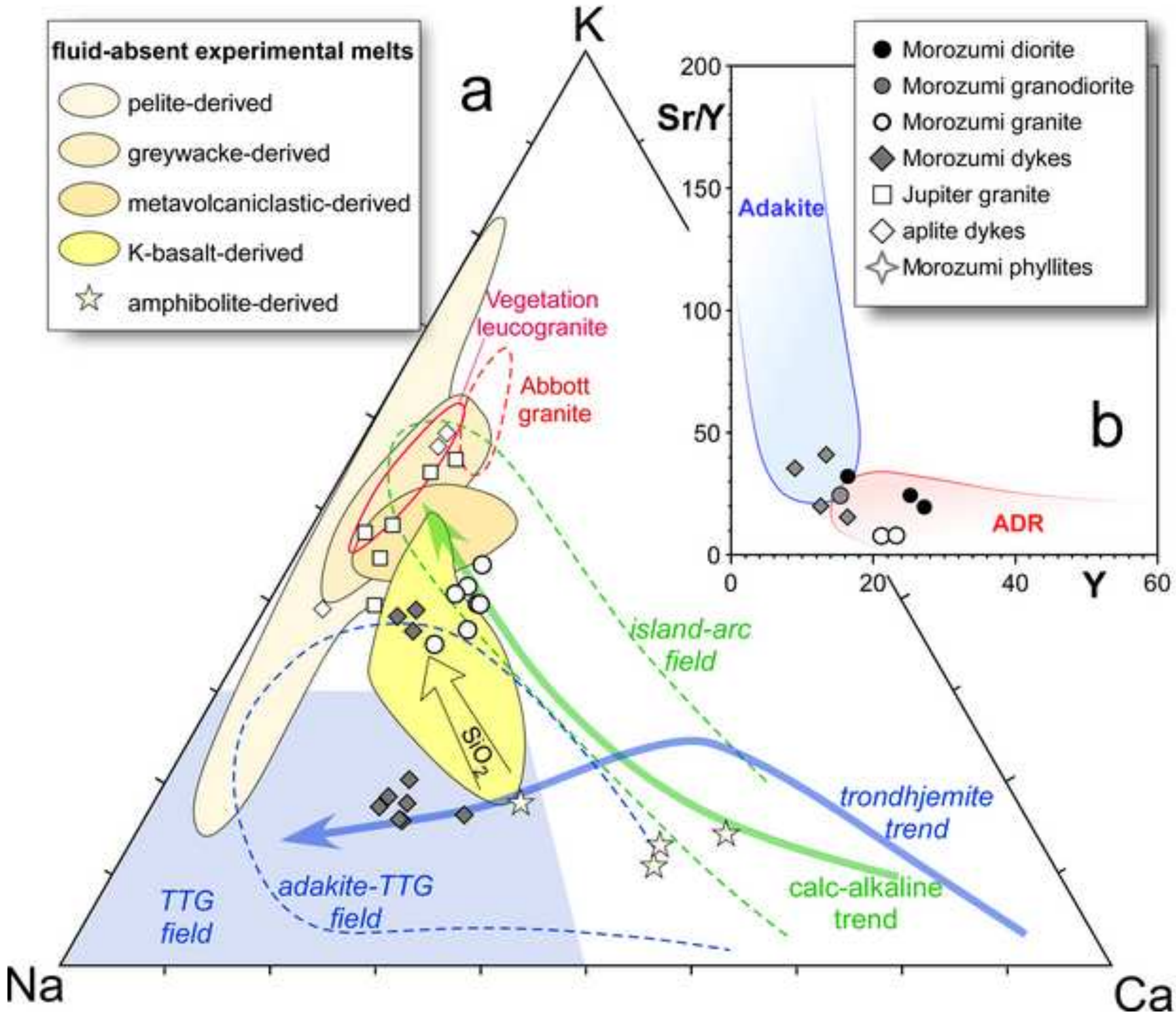

Figure 9
Click here to download high resolution image

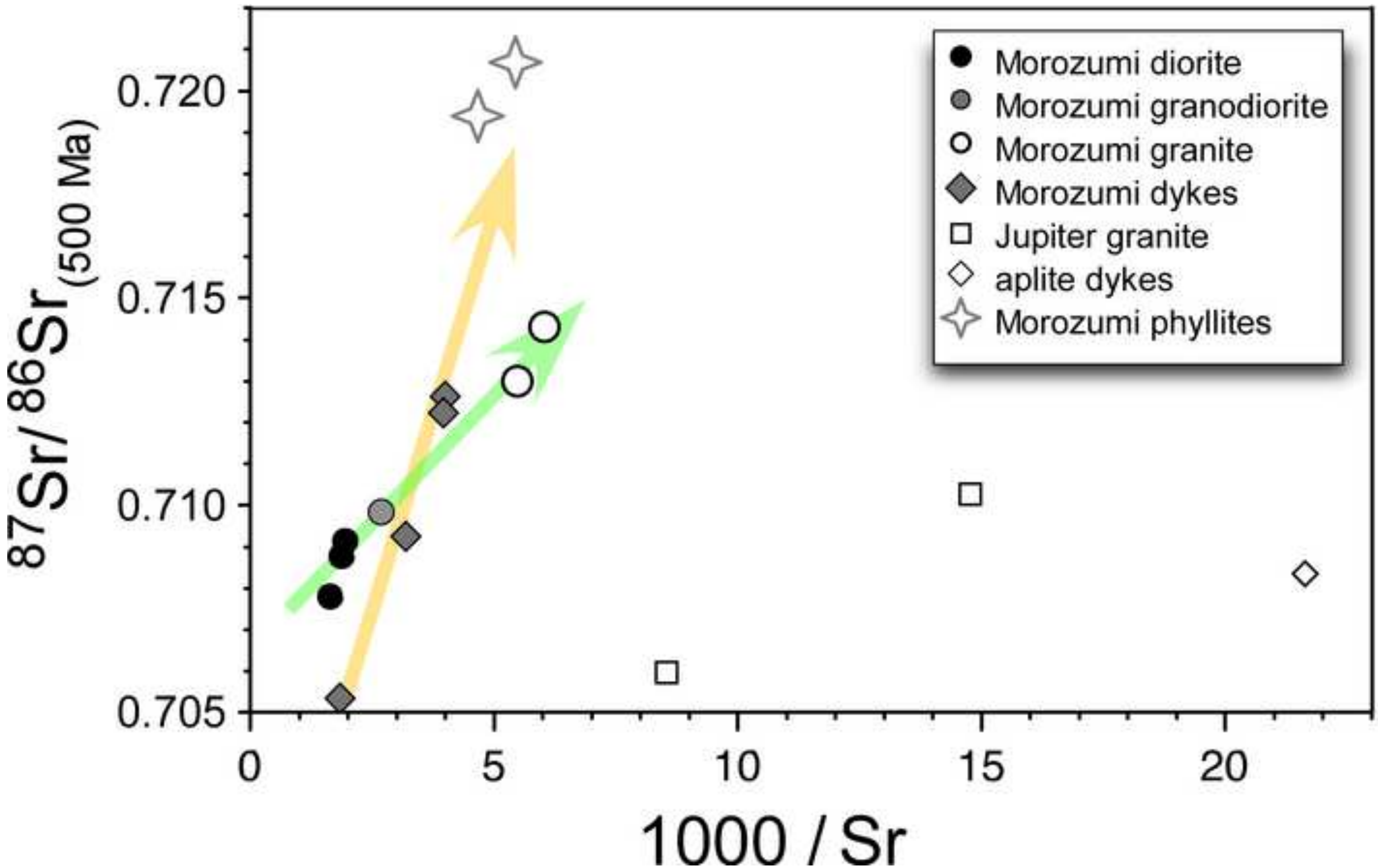

Figure 10
Click here to download high resolution image

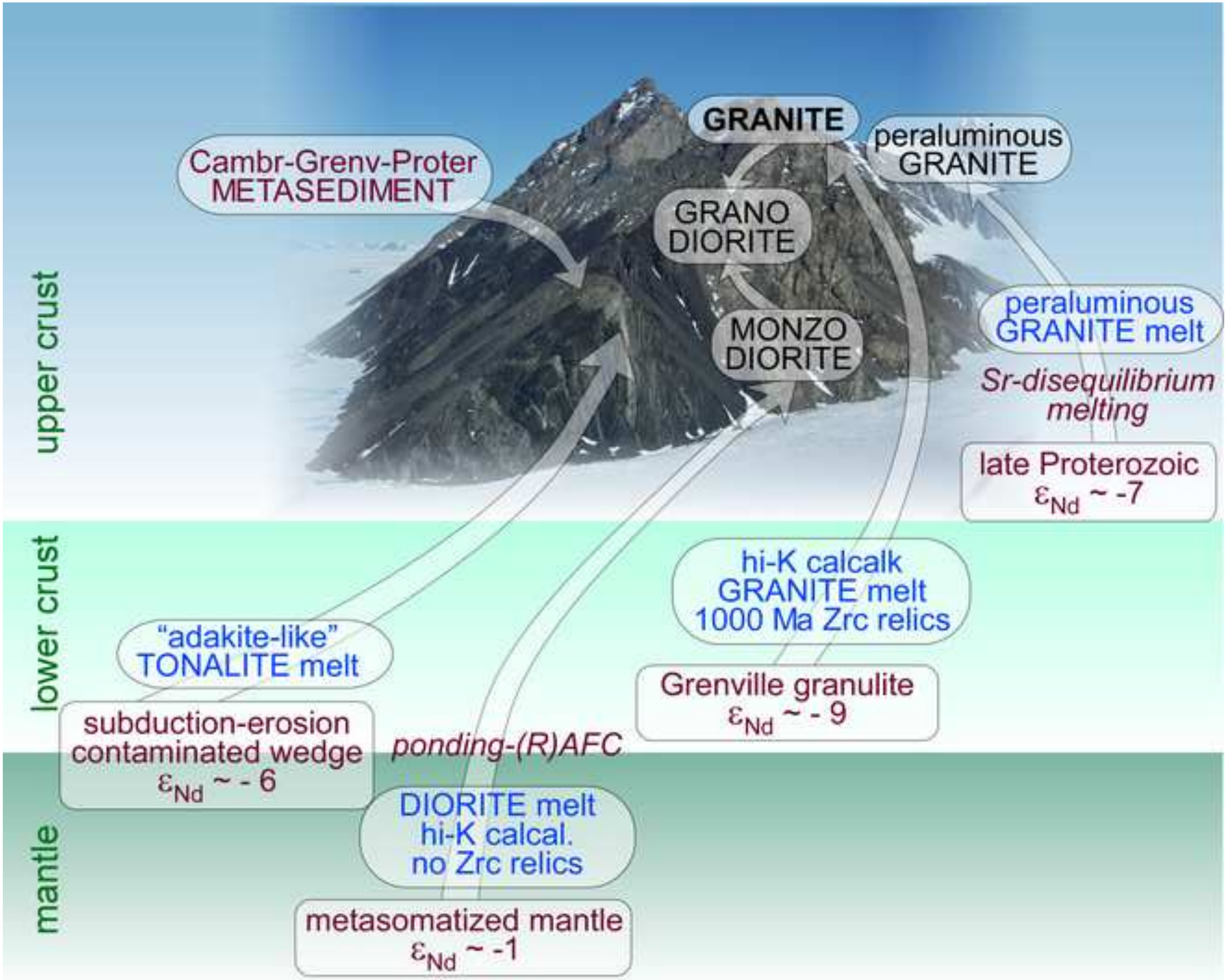

Table 1
Click here to download Table: Table 1 revised.xlsx

Table 1. Summary of field, petrographic and geochronological features of the lithologic units of the Morozumi Range intrusive complex.

unit	sub-unit	rock type	petrography	structure	field chronology relative to Morozumi granite	age (Ma)
Morozumi phyllites				vertical foliation	earlier	
Morozumi granite		monzogranite	Kfs-phyric, medium-grained, bt-bearing	Kfs-phyric, vertical foliation		494 ± 9
Morozumi diorite		quartzdiorite	fine- to medium-grained, bt+amph-bearing	isotropic	coeval (hot, ductile contacts)	
Morozumi granodiorite		granodiorite	fine-grained	isotropic	coeval (diffuse contact)	485 ± 5
Morozumi dykes	eastern	tonalite-granodiorite	medium-grained, bt+ms-bearing	foliated	early-coeval (flattened)	497 ± 7
	western	tonalite-granodiorite	fine or medium-grained, bt±ms-bearing		late (crosscut granite foliation, ductile reationships)	
	crestal	leucomonzogranites - leucogranodiorites	bt±ms-bearing		post (crosscut granite foliation, brittle reationships)	
Jupiter granite		monzogranite	medium- to coarse-grained, leucocratic, bt+ms-bearing	isotropic	unknown	495 ± 6
Morozumi leucogranites/aplites		leucogranite	fine- to medium-grained, ms ± grt/tur-bearing		late	

Table 2a
Click here to download Table: Table 2a revised.xlsx

Table 2. Major elements, trace elements and Sr-Nd isotopic data.

unit	Morozumi diorite						Mor. granodiorite		Morozumi granite						Morozumi phyllites	
sample	23.12.05 DS10	23.12.05 DS7	23.12.05 DS12	23.12.05 DS9	23.12.05 DS13	23.12.05 DS11	22.12.05 DS7	22.12.05 DS6	19.12.05 DS5	20.12.05 DS1	21.12.05 BS4	23.12.05 DS6	18.12.05 DS11	23.12.05 DS5	19.12.05 DS2	23.12.05 DS14
lat	71° 32.9'	71° 32.9'	71° 32.9'	71° 32.9'	71° 32.9'	71° 32.9'	71° 32.1	71° 32.1'	71° 27.08'	71° 26.9'	71° 28.3'	71° 32.9'	71° 29.9'	71° 32.2'	71° 46.8'	71° 33.2'
long	161° 37.7'	161° 37.7'	161° 37.7'	161° 37.7'	161° 37.7'	161° 37.7'	161° 38.7'	161° 38.7'	161° 42.0'	161° 49.9'	161° 44.3'	161° 37.7'	161° 44.9'	161° 43.0'	162° 10.9'	161° 47.8'
rock type	QD	QD	QD	MD	QMD	T	GD	GD	MG	MG	MG	MG	MG	MG		
Major elements (wt%)																
SiO_2	56.63	56.86	57.55	59.63	59.90	60.26	60.57	62.79	64.96	66.57	67.46	67.85	68.53	69.40	69.27	69.74
TiO_2	0.95	1.30	0.88	0.91	0.80	0.75	0.91	0.81	0.74	0.56	0.59	0.58	0.57	0.56	0.63	0.61
Al_2O_3	14.81	14.95	15.11	17.97	15.65	15.31	16.93	16.60	15.92	15.58	15.24	14.93	14.94	14.83	12.93	12.98
Fe_2O_3	6.82	8.52	6.52	6.10	5.88	5.84	5.88	5.19	4.62	3.19	3.80	3.71	3.52	3.58	4.01	5.36
MnO	0.11	0.13	0.09	0.09	0.09	0.10	0.07	0.07	0.07	0.06	0.07	0.06	0.06	0.06	0.05	0.07
MgO	6.32	4.82	5.46	3.04	4.80	5.17	2.76	2.30	1.51	1.13	1.22	1.23	1.16	1.17	2.18	2.68
CaO	6.81	6.22	6.22	4.92	5.84	5.84	4.54	4.27	2.27	2.59	2.64	2.40	2.64	2.59	1.36	2.02
Na_2O	2.85	2.84	2.81	3.33	3.06	2.90	2.97	3.01	3.09	3.01	2.99	3.01	2.98	3.04	1.69	2.83
K_2O	1.91	1.73	2.12	2.65	2.26	2.00	2.80	2.99	4.51	5.25	4.41	4.66	4.41	3.94	6.17	2.47
P_2O_5	0.53	0.60	0.31	0.36	0.29	0.31	0.36	0.29	0.34	0.18	0.21	0.19	0.20	0.20	0.20	0.16
LOI	1.96	1.97	1.87	1.78	1.66	1.58	1.40	1.99	1.99	0.87	1.17	0.88	0.69	1.18	1.07	1.18
Trace elements (ppm)																
Be	5.6	3.7		5.2			3.1					9.1	9.3		3.9	4.2
Sc	18.0	11.9		12.2			12.3					9.4	9.4		10.4	11.8
V	133.2	156.2		108.2			112.4					53.7	54.4		64.3	83.6
Cr	161.2	60.6		29.0			42.5					18.7	25.8		70.9	67.7
Co	26.7	24.8		15.6			15.2					7.2	7.4		10.0	12.3
Ni	124.7	38.9		19.1			26.1					8.6	7.9		26.5	31.1
Cu	36.9	20.3		51.5			34.8					10.9	19.7		5.0	32.0
Ga	18.4	17.7		21.3			21.8					19.8	19.3		15.9	17.3
Rb	134.6	119.6		165.5			165.0					260.4	244.4		185.5	142.4
Sr	610.6	526.0		528.1			373.8					183.0	165.7		214.6	183.8
Y	25.19	27.10		16.45			15.33					23.21	21.11		29.00	31.32
Zr	173	226		240			266					214	192			
Nb	9.33	12.75		11.42			12.91					15.92	16.31		12.72	13.10
Cs	15.64	19.06		18.60			7.53					24.69	44.92		18.35	11.76
Ba	312.3	714.9		444.0			501.5					526.5	543.1		845.2	318.9
La	46.82	59.75		48.36			61.94					58.40	46.14		50.24	31.51
Ce	110.65	135.24		100.74			129.26					123.03	97.21		102.58	65.61
Pr	14.79	16.82		11.48			14.83					14.20	11.26		11.94	7.80
Nd	60.46	65.42		40.87			53.16					50.28	40.49		44.10	29.21
Sm	11.13	11.70		6.61			8.45					9.25	7.54		7.99	6.12
Eu	2.27	2.43		1.33			1.32					1.27	1.27		1.36	1.13
Gd	7.76	8.51		4.75			5.76					6.55	5.51		6.36	5.37
Tb	0.94	1.13		0.65			0.70					0.88	0.78		0.94	0.83
Dy	4.81	5.57		3.23			3.20					4.53	3.92		5.20	5.04
Ho	0.87	1.00		0.60			0.56					0.83	0.75		1.03	1.07
Er	2.18	2.48		1.54			1.37					2.06	1.83		2.70	2.90
Tm	0.31	0.33		0.21			0.19					0.29	0.27		0.39	0.45
Yb	1.89	1.99		1.31			1.15					1.82	1.60		2.43	2.68
Lu	0.26	0.28		0.20			0.16					0.26	0.22		0.34	0.38
Hf	2.58	5.01		3.17			3.16					4.96	4.36		4.08	3.55
Ta	1.12	0.88		1.02			0.79					1.74	2.25		1.11	1.12
Tl	1.03	0.90		1.65			1.27					1.80	1.64		1.18	1.03
Pb	8.22	13.00		11.73			13.40					37.47	36.49		38.08	28.88
Th	10.98	11.73		12.06			17.11					27.04	20.76		17.90	11.90
U	3.69	4.93		3.63			1.24					4.41	2.56		2.32	2.76
Sr-Nd isotope data																
$^{87}Sr/^{86}Sr$	0.712345	0.713517		0.715543			0.718944					0.742427	0.744825		0.737277	0.736718
error (2s)	0.000070	0.000011		0.000011			0.000012					0.000012	0.000012		0.000010	0.000080
$^{87}Rb/^{86}Sr$	0.638	0.658		0.907			1.279					4.131	4.283		2.508	2.248
$^{87}Sr/^{86}Sr_{(500Ma)}$	0.707798	0.708826		0.709079			0.709833					0.712995	0.714309		0.719403	0.720700
$\varepsilon_{Sr(500Ma)}$	55	70		73			84					129	148		220	238
$^{143}Nd/^{144}Nd$	0.512143	0.512130		0.512002			0.511873					0.511881	0.511880		0.511798	0.511922
error (2s)	0.000007	0.000007		0.000007			0.000006					0.000007	0.000005		0.000007	0.000007
$^{147}Sm/^{144}Nd$	0.1112	0.1081		0.0977			0.0961					0.1112	0.1126		0.1095	0.1266
$^{143}Nd/^{144}Nd_{(500}$	0.511779	0.511776		0.511682			0.511558					0.511517	0.511511		0.511439	0.511507
$\varepsilon_{Nd(500Ma)}$	-4.2	-4.3		-6.1			-8.5					-9.3	-9.4		-10.8	-9.5
T_{DM} (Ga)	1.55	1.55		1.68			1.85					1.91	1.92		2.01	1.92

Rock name abbreviations: D: diorite, MD: monzodiorite, QD: quartz diorite, QMD: quartz monzodiorite, T: tonalite, GD: granodiorite, MG: monzogranite, SG: syenogranite, AFG: alkali feldspar granite. Igneous rock names according to Q'-ANOR diagram after Streckeisen et al. (1978). T_{DM}: Nd model age calculated according to DePaolo et al. (1991)

Table 2b

Click here to download Table: Table 2b revised.xlsx

Table 2 (ctd)**.** Major elements, trace elements and Sr-Nd isotopic data.

unit	Mor. dykes-easterr		Morozumi dykes-western				Morozumi dykes-crestal					Jupiter granite						aplites-leucogranites		
sample	18.12.05 DS7	21.12.05 BS1	20.12.05 DS4	20.12.05 DS2	23.12.05 DS2	23.12.05 DS3	22.12.05 DS1m	21.12.05 BS7	21.12.05 BS5	22.12.05 DS1l	21.12.05 BS6	20.12.05 DS3	23.12.05 DS4	23.12.05 DS1	22.12.05 DS3	20.12.05 DS6	23.12.05 DS15	23.12.05 DS8	18.12.05 DS9	18.12.05 DS10
lat	71° 26.5'	71° 26.6'	71° 27.3'	71° 26.9'	71° 29.9'	71° 29.9'	71° 28.3'	71° 28.3'	71° 28.3'	71° 28.3'	71° 28.3'	71° 27.3'	71° 31.7'	71° 29.9'	71° 19.3'	71° 34.9'	71° 30.6'	71° 32.9'	71° 26.5'	71° 26.5'
long	161° 43.0'	161° 50.6'	161° 41.9'	161° 49.9'	161° 41.9'	161° 41.9'	161° 44.3'	161° 44.3'	161° 44.3'	161° 44.3'	161° 44.34	161° 41.9'	161° 41.1'	161° 41.9'	161° 19.7'	161° 50.6'	161° 44.7'	161° 37.7'	161° 43.0'	161° 43.0'
rock type	GD	T	T	T	GD	T	GD	GD	MG	MG	MG	MG	SG	SG	SG	MG	SG	AFG	SG	SG
Major elements (wt%)																				
SiO_2	70.38	70.44	64.75	68.28	69.64	71.41	70.73	70.87	72.76	73.31	73.92	72.27	72.58	73.16	73.67	74.19	74.28	74.54	74.67	75.20
TiO_2	0.30	0.29	0.49	0.37	0.40	0.37	0.29	0.29	0.20	0.18	0.19	0.28	0.17	0.16	0.35	0.13	0.13	0.10	0.03	0.03
Al_2O_3	15.29	14.92	16.53	15.92	15.31	15.07	14.77	14.95	13.82	14.10	13.99	14.08	14.37	14.23	12.26	13.91	13.67	13.86	13.82	14.49
Fe_2O_3	2.61	2.53	4.48	3.41	3.25	2.99	2.72	2.86	1.79	1.50	1.69	1.68	1.25	1.29	2.41	1.23	1.33	0.97	0.48	0.31
MnO	0.05	0.05	0.08	0.06	0.05	0.04	0.04	0.05	0.03	0.03	0.03	0.04	0.03	0.02	0.04	0.04	0.05	0.03	0.01	0.06
MgO	1.26	0.95	2.47	1.44	1.08	0.93	0.84	0.76	0.60	0.50	0.56	0.61	0.36	0.55	0.76	0.30	0.36	0.24	0.14	0.11
CaO	2.86	3.02	4.76	3.70	2.92	2.93	2.70	2.79	1.80	1.83	1.60	1.31	0.97	1.12	0.86	1.19	0.98	0.73	1.04	0.69
Na_2O	4.48	4.07	1.90	3.63	3.92	4.02	4.07	3.82	3.20	3.35	3.40	2.59	3.25	2.92	2.24	3.34	3.24	3.74	2.60	4.12
K_2O	1.93	1.64	2.43	1.69	1.81	1.63	1.91	2.07	3.69	4.23	4.03	6.22	5.34	6.28	5.42	3.96	4.62	5.66	6.72	4.40
P_2O_5	0.11	0.10	0.10	0.11	0.17	0.10	0.12	0.11	0.09	0.10	0.10	0.14	0.20	0.14	0.10	0.08	0.18	0.08	0.08	0.10
LOI	1.21	1.66	2.25	1.19	0.93	0.78	1.17	0.96	1.23	1.50	1.09	1.24	0.86	1.27	0.95	1.61	1.04	0.89	0.79	0.94
Trace elements (ppm)																				
Be	3.1			3.2			4.3			5.5			7.3			10.6				6.3
Sc	6.5			7.1			5.7			4.2			3.4			5.3				2.5
V	36.7			41.2			22.1			10.5			7.2			9.4				0.6
Cr	32.6			36.1			10.0			7.3			6.8			5.7				4.7
Co	6.4			8.1			3.9			2.2			1.4			1.2				0.3
Ni	14.2			11.4			4.6			2.5			2.0			1.6				0.6
Cu	2.4			9.3			2.6			2.3			9.9			1.1				0.6
Ga	17.6			14.9			18.3			14.9			19.7			15.8				13.0
Rb	84.0			135.3			132.8			171.6			365.2			195.3				161.1
Sr	547.2			313.8			251.7			251.0			67.6			117.1				46.2
Y	13.41			8.94			12.59			16.34			13.12			25.13				12.40
Zr	133			122			143			99			87			72				28
Nb	5.79			6.63			15.66			10.07			17.16			11.23				7.12
Cs	8.95			17.25			8.68			5.88			20.48			17.03				4.85
Ba	406.3			288.5			212.6			660.1			213.7			405.8				248.9
La	21.16			20.11			28.22			29.86			22.76			16.48				5.68
Ce	42.83			37.60			54.40			57.03			49.34			34.65				12.41
Pr	4.87			3.90			5.93			6.17			5.74			4.07				1.46
Nd	18.11			13.61			20.54			21.10			20.61			15.00				5.43
Sm	3.73			2.17			3.43			3.80			4.70			3.29				1.78
Eu	0.66			0.70			0.76			0.80			0.54			0.60				0.16
Gd	3.18			1.87			2.74			3.02			3.70			3.08				1.64
Tb	0.49			0.28			0.40			0.46			0.54			0.58				0.32
Dy	2.47			1.57			2.16			2.55			2.63			3.60				1.89
Ho	0.46			0.30			0.41			0.53			0.42			0.80				0.39
Er	1.20			0.83			1.13			1.50			0.95			2.30				1.14
Tm	0.20			0.13			0.17			0.22			0.14			0.38				0.19
Yb	1.23			0.78			1.14			1.37			0.85			2.49				1.26
Lu	0.16			0.12			0.17			0.21			0.11			0.36				0.17
Hf	0.77			1.63			3.14			2.19			2.62			1.91				0.99
Ta	0.85			0.80			1.68			1.18			2.03			2.44				1.61
Tl	0.64			1.17			0.99			1.09			2.27			1.29				0.94
Pb	11.42			10.59			20.69			34.95			42.01			34.31				25.32
Th	6.98			5.26			8.86			10.98			12.84			8.14				1.91
U	0.62			26.50			2.24			2.63			3.72			2.96				1.37
Sr-Nd isotope data																				
$^{87}Sr/^{86}Sr$	0.708517			0.718166			0.723144			0.726733			0.822843			0.740428				0.780698
error (2s)	0.000009			0.000008			0.000011			0.000009			0.000011			0.000009				0.000010
$^{87}Rb/^{86}Sr$	0.444			1.249			1.529			1.982			15.801			4.842				10.157
$^{87}Sr/^{86}Sr_{(500Ma)}$	0.705351			0.709270			0.712250			0.712614			0.710254			0.705927				0.708328
$\varepsilon_{Sr(500Ma)}$	20			76			118			124			90			29				63
$^{143}Nd/^{144}Nd$	0.512045			0.512023			0.511982			0.511873			0.511926			0.512000				0.512222
error (2s)	0.000007			0.000008			0.000007			0.000008			0.000009			0.000006				0.000009
$^{147}Sm/^{144}Nd$	0.1246			0.0965			0.1008			0.1089			0.1378			0.1325				0.1986
$^{143}Nd/^{144}Nd_{(500}$	0.511637			0.511707			0.511652			0.511516			0.511475			0.511566				0.511572
$\varepsilon_{Nd(500Ma)}$	-7.0			-5.6			-6.7			-9.3			-10.1			-8.4				-8.2
T_{DM} (Ga)	1.75			1.65			1.73			1.91			1.96			1.84				1.84